

Thermodynamic state retrieval from microwave occultation data and performance analysis based on end-to-end simulations

S. Schweitzer,¹ G. Kirchengast,¹ M. Schwaerz,¹ J. Fritzer,¹ and M. E. Gorbunov^{1,2}

Received 31 July 2010; revised 15 February 2011; accepted 18 February 2011; published 18 May 2011.

[1] Microwave occultation using centimeter- and millimeter-wave signals between low Earth orbit (LEO) satellites (LEO microwave occultation, LMO) is an advancement of GPS radio occultation (GRO) exploiting in addition to refraction also absorption of signals. Beyond the successful GRO refractivity profiling capability, which leaves a temperature-humidity ambiguity in the troposphere where moisture cannot be neglected, LMO enables joint retrieval of pressure, temperature, and humidity profiles without auxiliary background information. Here we focus on the upper troposphere/lower stratosphere and advance the LMO method in two ways: (1) we introduce a new retrieval algorithm for processing LMO excess phase and amplitude data from multiple frequencies, complementing existing GRO retrieval algorithms, and (2) we employ the algorithm in an ensemble-based end-to-end performance analysis and assess the accuracy of pressure, temperature, and humidity profiles retrieved from the LMO data. The end-to-end simulations were carried out under quasi-realistic conditions for a day of LEO-LEO occultation events, based on a high-resolution atmospheric analysis of the European Centre for Medium-Range Weather Forecasts (ECMWF) and accounting for scintillation noise from turbulence and instrumental errors. The new algorithm was found robust, fast, and versatile to adequately process LMO data under all conditions from dry and clear to moist and cloudy air as contained in the ECMWF analysis. The retrieved pressure, temperature, and humidity profiles were generally found unbiased and within target accuracy requirements, set by scientific objectives of atmosphere and climate research going to be supported by the data, of <0.2% (pressure), <0.5 K (temperature), and <10% (humidity). Extending a “minimum” LMO design with three frequencies near 22 GHz with two added frequencies near 183 GHz favorably provides humidity retrieval into the lower stratosphere but already the “minimum” design resolves the temperature-humidity ambiguity of GRO in the upper troposphere (frequencies <15 GHz might extend this into the lower troposphere). The results are encouraging for future LMO implementation, both stand-alone and combined with novel LEO-LEO infrared laser occultation.

Citation: Schweitzer, S., G. Kirchengast, M. Schwaerz, J. Fritzer, and M. E. Gorbunov (2011), Thermodynamic state retrieval from microwave occultation data and performance analysis based on end-to-end simulations, *J. Geophys. Res.*, 116, D10301, doi:10.1029/2010JD014850.

1. Introduction

[2] The microwave occultation technique using inter-satellite centimeter- and millimeter-wave signals between low Earth orbit (LEO) satellites [Kursinski *et al.* 2002, 2004; Herman *et al.*, 2004; Kirchengast and Hoeg, 2004; Gorbunov and Kirchengast, 2005, 2007], termed LMO hereafter, enables us to jointly retrieve atmospheric profiles of temperature and humidity without auxiliary background

information, in addition to profiles of refractivity, pressure, and geopotential height. LMO thus allows retrieval of all fundamental thermodynamic state variables (pressure, temperature, and humidity), as a function of height, and with added dedicated signals also other variables, in particular ozone [Herman *et al.*, 2004]. This is a key advancement compared to the highly successful radio occultation technique utilizing decimeter-wave signals from the Global Navigation Satellite System (GNSS) received at LEO satellites [e.g., Ware *et al.*, 1996; Kursinski *et al.*, 1997; Steiner *et al.*, 1999; Wickert *et al.*, 2004; Healy and Thépaut, 2006; Anthes *et al.*, 2008; Ho *et al.*, 2009; Steiner *et al.*, 2009], termed GRO hereafter (up to present the GNSS signals exploited were those from the U.S. Global Positioning System GPS). GRO allows retrieval of temperature and humidity only using prior information because

¹Wegener Center for Climate and Global Change and Institute for Geophysics, Astrophysics, and Meteorology/Institute of Physics, University of Graz, Graz, Austria.

²Institute of Atmospheric Physics, Russian Academy of Sciences, Moscow, Russia.

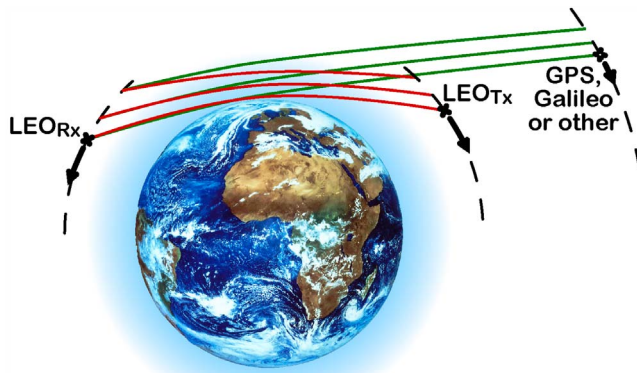


Figure 1. Schematic view of the LEO-LEO (red signal paths) and GNSS-LEO (green signal paths) occultation event geometry.

of a temperature-humidity ambiguity in refractivity [Smith and Weintraub, 1953], which is the fundamental variable derived from GRO data. Both LMO and GRO share the unique combination of properties that the occultation measurement principle provides [Kirchengast, 2004], including high accuracy and vertical resolution, long-term stability, nearly all-weather capability and global coverage [e.g., Kursinski et al., 1997]. Figure 1 illustrates the geometrical setup of LMO and GRO; Kirchengast and Hoeg [2004] provide a detailed overview description for both techniques, with emphasis on the new LMO method.

[3] The reason why temperature and humidity can be simultaneously retrieved from LMO data is that LMO exploits frequencies at the wings and near the line center of absorption lines of water vapor. Therefore there is sensitivity to both refraction and absorption, while the GRO frequencies in L band (1 to 2 GHz) are only sensitive to refraction (except in the lower troposphere toward the surface where some absorption may occur [e.g., Kursinski et al., 2000]). In particular, frequencies around the water vapor absorption lines at 22 GHz and 183 GHz, and the 195 GHz ozone line, have been investigated by Kursinski et al. [2002], Herman et al. [2004], and Kirchengast and Hoeg [2004], which are also the starting point for this study. The integrated absorption, and subsequently the absorption coefficient profile, is determined from the observed amplitude attenuation of each transmitted signal during the occultation event. Together the signals at all frequencies provide an accurate constraint on the water vapor profile probed during the event. In combination with the refractivity measured in the same way as done by GRO, LMO can thus simultaneously furnish pressure, temperature, and humidity.

[4] Whereas GRO has already been well established by a variety of satellite missions (GPS/MET [Rocken et al., 1997], CHAMP [Wickert et al., 2004], SAC-C [Hajj et al., 2004], GRACE [Beyerle et al., 2005], COSMIC [Anthes et al., 2008], and MetOp/GRAS [Luntama et al., 2008]), LMO was only investigated theoretically and by simulation studies so far. The first proposed LMO concept dates back to Lusignea et al. [1969]. They did not aim to provide highly resolved vertical scans of the atmosphere during occultation events but proposed a significant number (>10) of corotating

satellites to measure at a few height levels (also termed “spinmap concept”). It then took about 3 decades, and the intermediate advent of GRO as of the late 1980s, until the first LMO concepts with GRO-type geometry (i.e., with fast near-vertical scanning via transmitter and receiver satellite motion) had been proposed. These were described by Yunck et al. [2000], Kursinski et al. [2002, 2004], and Herman et al. [2004] for U.S.-led (NASA) concepts and by Kirchengast and Hoeg [2004] for European-led (European Space Agency, ESA) concepts.

[5] While by mid-2010 no LMO mission was put on a firm track to full realization yet, activities past 2004 have led to fruitful further developments building on these previous concepts. The current U.S.-led mission concept is the Active Temperature, Ozone, and Moisture Microwave Spectrometer (ATOMMS), a prototype of which is being prepared in NSF/NASA context for a stratospheric airplane-to-airplane demonstration experiment of LMO [Kursinski et al., 2009]. The current European-led concept is the ACCURATE—Climate Benchmark Profiling of Greenhouse Gases and Thermodynamic Variables and Wind from Space mission concept [Kirchengast et al., 2010], combining LMO with a novel infrared laser occultation approach for profiling greenhouse gases and wind. This mission concept is currently under scientific study and technological predevelopment in ESA context [Kirchengast et al., 2010; Schweitzer, 2010; Larsen et al., 2009; G. Kirchengast and S. Schweitzer, submitted manuscript, 2011].

[6] This study provides an essential contribution to understanding and exploiting the utility of LMO in the atmospheric sciences in that it (1) introduces a robust thermodynamic state retrieval algorithm for LMO data, advancing existing GRO retrieval algorithms [Kursinski et al., 1997; Ho et al., 2009, and references therein]; and (2) uses the algorithm in an ensemble-based end-to-end performance analysis that assesses the accuracy of pressure, temperature, and humidity profiles retrieved from LMO data, advancing existing estimates from previous LMO work. The performance results are put into context with LMO observational requirements [European Space Agency (ESA), 2004a, 2004b; Larsen et al., 2009] which have been defined in a way so that the scientific objectives of contributing to atmosphere and climate research [Kirchengast and Hoeg, 2004; Kursinski et al., 2009; Larsen et al., 2009] can be met.

[7] The paper is structured as follows. Section 2 presents the new LMO thermodynamic state retrieval algorithm, with focus on the extensions built on top of existing GRO algorithms. Section 3 describes the design of the end-to-end simulations used for the performance analysis, and section 4 shows and discusses the analysis results. Finally, section 5 provides a summary and conclusions.

2. Retrieval Algorithm

2.1. Overview of the LMO Retrieval

[8] The performance analysis in this study specifically considers LMO, which uses an occultation geometry with transmitter and receiver satellites in LEO as illustrated in Figure 1. However, the retrieval algorithm introduced here is valid for every transmitter-receiver setup providing occultation geometry, e.g., also for using transmitters in the

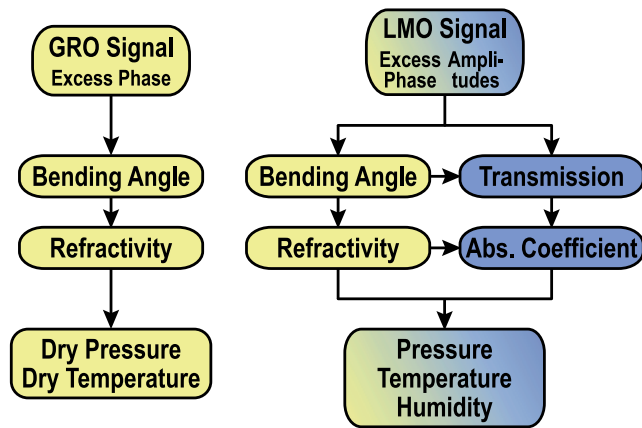


Figure 2. Schematic comparison of the retrieval processing using (left) GRO and (right) LMO signals.

higher GNSS orbits (coindicated in Figure 1) if some future GNSS satellites would include additional microwave signals [Schwaerz et al., 2006] or using the receiver (and optionally transmitter) on airplane [Lesne et al., 2002; Kursinski et al., 2009]. The focus on LMO as the preferred geometry is due to the favorable signal-to-noise ratio achievable by the relatively short transmitter-receiver distances (about 6,000 km, compared to about 30,000 km in GRO-type setups) while at the same time reaching global coverage, possible only when both transmitter and receiver reside in space (i.e., at least at LEO heights).

[9] Figure 2 shows an overview diagram of the LMO retrieval chain compared to the well known GRO (dry air) retrieval chain. The latter is primarily based on the atmospheric excess phase of GNSS signals from which the atmospheric variables are derived via the intermediate steps of bending angle and refractivity retrieval [e.g., Kursinski et al., 1997; Gorbunov, 2002; Gorbunov and Lauritsen, 2004; Jensen et al., 2003, 2004]. From the right-hand side of Figure 2 one can see that the amplitude (attenuation) data, available for each absorption-sensitive microwave frequency chosen, are the key added ingredient of LMO. From these amplitudes, transmission profiles can be retrieved in addition to the bending angle, and absorption coefficient profiles in addition to the refractivity. The joint availability of both refractivity and absorption coefficient profiles then allows us to unambiguously derive the thermodynamic state profiles of pressure, temperature, and humidity.

[10] For providing sufficient practical utility, we generally follow with the algorithm description below the actual implementation as we put it into the End-to-End Generic Occultation Performance Simulation and Processing System version 5 (EGOPS5) software [Kirchengast et al., 2007; Fritzer et al., 2010], where it is part of the Occultation Processing System component, current version 5.5 (OPS 5.5). For brevity we refer to this implementation simply as OPS or OPS processing hereafter. For bending angle and transmission retrieval we restrict on describing the geometric optics retrieval, since the wave optics retrieval has already been described and applied elsewhere [Gorbunov, 2002; Jensen et al., 2003; Gorbunov and Lauritsen, 2004; Nielsen et al., 2005; Gorbunov and Kirchengast, 2005, 2007]. Also for the performance analysis (sections 3 and 4)

we use the geometric optics retrieval of bending angle and transmission profiles.

[11] Having Figure 2 as guideline, the retrieval chain can be summarized as follows, before detailing the new LMO-specific parts: First, shared with GRO retrieval, bending angle is derived as a function of impact parameter from excess phase measurements and precise orbit determination (POD) data, which comprise velocity and position vectors of the transmitter and receiver satellites. This process includes smoothing of excess phase data in order to avoid unnecessary amplification of high-frequency noise (over about 1 s, corresponding to about 2 km in height, less below about 35 km), ionospheric correction of phases or bending angles, and statistical optimization of the retrieved bending angle at high altitudes [Gobiet and Kirchengast, 2004; Gobiet et al., 2007; Steiner et al., 2009]. Second, LMO-specific, transmissions are computed as a function of impact parameter from the amplitudes of all chosen signal frequencies, using the impact parameter from the bending angle retrieval and POD data. Since the amplitudes are influenced by defocusing and spreading, these effects are eliminated to obtain the transmissions caused by absorption only. Differential transmissions between adjacent frequencies are then computed as well; they can also serve as basic transmission quantity for the subsequent retrieval. Third, again equal to the GRO, the bending angle as a function of impact parameter is converted to the refractivity as a function of height via the well known Abel transform [e.g., Fjeldbo et al., 1971; Kursinski et al., 1997; Rieder and Kirchengast, 2001]. The upper limit of this Abel integral is set to a height of 120 km, which ensures high quality of the refractivity retrieval throughout the stratosphere and below [Steiner et al., 1999, 2009].

[12] The remaining steps are LMO-specific. Fourth, volume absorption coefficients as a function of height are derived from transmissions via another Abel transform [e.g., Kursinski et al., 2002] (for brevity referred to just as absorption coefficients hereafter), using also refractivity and impact parameter. Fifth and finally, refractivity and absorption coefficients are used, together with equations constraining the atmospheric state variables pressure, temperature, humidity, optionally ozone, and cloud liquid water, in order to retrieve profiles of these state variables as function of height. The equations involved in this process are the refractivity equation (Smith-Weintraub formula [Smith and Weintraub, 1953]), hydrostatic equation, equation-of-state including formulae for virtual temperature and specific humidity, and spectroscopic equations for computing the frequency-dependent absorption coefficient from the atmospheric variables (in OPS an enhanced version of the Liebe Model [Liebe et al., 1993]). The state variables are estimated via downward integration (in height) of the hydrostatic equation, combined with an iterative Best Linear Unbiased Estimation (BLUE) [Rodgers, 2000] solution at each integration step. The BLUE algorithm requires specification of error covariance matrices for refractivity and absorption coefficients and becomes effectively underdetermined if the errors of absorption coefficients grow too large, corresponding to effectively reducing the number of useful measurements. In this case, adequate prior temperature information including its error is being used, at heights below 3 to 7 km, to ensure accurate estimation of the state variables.

[13] In the following subsections, the LMO-specific algorithm steps (2, 4, and 5 above) are explained in detail, based on relevant parts of a report by *Kirchengast et al.* [2006] and with updates to reflect the current OPS. A basic original version starting with wave optics retrieval was described in a report by *Gorbunov et al.* [2007]. The steps shared with GRO (steps 1 and 3) are not further detailed here since already described in the references cited above (and as well in detail by *Kirchengast et al.* [2006]).

2.2. Transmission Retrieval

[14] Transmission is defined as the ratio of attenuated signal intensity I after passing the atmosphere to unattenuated intensity I_0 above the atmosphere (practically, I_0 at a reference height z_{ref} sufficiently high so that attenuation is negligible; note that this definition is slightly different from that of *Kursinski et al.* [2002]). Since intensity is proportional to amplitude-squared ($I \propto A^2$), transmission can be derived equivalently from amplitude measurements, if the unattenuated amplitude is known accordingly.

[15] The OPS retrieves transmission profiles as function of impact parameter a at each signal frequency j , $\mathcal{T}_j(a)$, where these express atmospheric absorption only (transmission = 1 – absorption). This absorption occurs at frequencies of primary LMO interest (centimeter waves in 8 to 30 GHz, millimeter waves in 175 to 200 GHz [e.g., *Herman et al.*, 2004]) due to water vapor and background air (molecular oxygen and nitrogen mainly), tropospheric clouds if present (liquid clouds mainly), and stratospheric ozone (within 190 to 200 GHz). In order to isolate the absorption-only transmission $\mathcal{T}_j(a)$, the retrieval corrects other effects that attenuate the amplitude, including defocusing loss due to differential bending and spherical signal spreading due to geometry. It normalizes the amplitude at any vertical level i , $A_j(a_i)$, to the unattenuated one at a suitable “top-of-atmosphere” impact height z_{ref} (impact height = a – Earth’s local radius of curvature; it is closely the same as height from 25 km upward as of interest here). We do have the input amplitude profiles $A_j(a)$ already available here as function of a , and not only of time t , since the geometric optics bending angle retrieval provided at every vertical level the a_i value at any time t_i .

[16] The amplitude deformation caused by defocusing and spreading, $A_{\text{ds}}(a_i)$, is, following *Jensen et al.* [2003], modeled as function of the impact parameter a , the radial distances from the center of Earth’s local curvature to the transmitter (T_x) and receiver (R_x) satellites, $r_{T_x}(a)$ and $r_{R_x}(a)$, and the opening angle between these two radius vectors, $\theta(a)$,

$$A_{\text{ds}}(a_i) = \left[\frac{a_i}{(r_{T_x} r_{R_x})^2 \sin \theta \sqrt{1 - \left(\frac{a_i}{r_{T_x}}\right)^2} \sqrt{1 - \left(\frac{a_i}{r_{R_x}}\right)^2} \left| \frac{d\theta}{da} \right|} \right]^{1/2}, \quad (1)$$

where all needed input parameters are available from the bending angle retrieval. Note that these refractive-geometric effects, and consequently $A_{\text{ds}}(a_i)$, do not depend on frequency. Equation (1) applies to a spherically symmetric atmosphere and circular and near-circular orbits, where a small delta-factor for radial changes ($\propto dr_{T_x}/d\theta$, $dr_{R_x}/d\theta$) is negligible. Other variants of this correction exist [e.g.,

Sokolovskiy, 2000], accounting also for radial changes (elliptical orbits), and different formulations apply to amplitudes from wave optics retrieval [*Jensen et al.*, 2003; *Gorbunov and Lauritsen*, 2004; *Nielsen et al.*, 2005]. Residual effects of deviations of the atmosphere from (local) spherical symmetry, i.e., of horizontal gradients, only cancel in differential transmissions between neighbor frequencies, computed as subsequent step below (in practice, if solely differential transmissions are needed, equation (1) can as well be bypassed since the frequency-independent $A_{\text{ds}}(a_i)$ cancels also due to the differencing).

[17] Using the defocusing and spreading amplitude deformation $A_{\text{ds}}(a_i)$ from equation (1) we can normalize it to align with the input amplitude $A_j(a_i)$ at reference height z_{ref} and then compute the ratio of both to obtain $\mathcal{T}_j(a)$. In the OPS this is formulated as

$$A_j^{\text{ds}}(a_i) = \left(\frac{A_j}{A_{\text{ds}}} \right)_{z_{\text{ref}}}^{\Delta z} \cdot A_{\text{ds}}(a_i), \quad (2)$$

$$\mathcal{T}_j^{\text{log}}(a_i) [\text{dB}] = -20 \cdot \left[\log A_j(a_i) - \log A_j^{\text{ds}}(a_i) \right], \quad (3)$$

where equation (2) performs the normalization aligning $A_{\text{ds}}(a_i)$ at any frequency j to the amplitude A_j at specified height $z_{\text{ref}j}$ and where equation (3) then uses $\log A_j^{\text{ds}}(a_i)$ as reference amplitude subtracted from the input amplitude $\log A_j(a_i)$ to obtain the desired (log-)transmission profile pertaining to absorption only (the subtraction in log-space corresponding to ratioing in linear space; in the OPS we primarily use log-transmission in units of dB, given the specific symbol \mathcal{T}^{log} here, which is proportional to the optical thickness). As seen in equation (2), the normalization factor is practically, for small-scale noise mitigation, not computed as a single-level quantity at $z_{\text{ref}j}$ but rather as a mean estimate over a height range Δz , applied as $z_{\text{ref}j} \pm \Delta z/2$, with Δz typically set to 4 km in OPS operations. In the OPS we also smooth a , $A_j(a)$, and $A_{\text{ds}}(a)$ by applying a moving third-order polynomial filter, with the width of the filtering polynomial set to about 1 km, before using a in equation (1) and the other two in equations (2) and (3). The resulting profiles $\mathcal{T}_j^{\text{log}}(a)$ are smoothed in the same way. This prevents the subsequent absorption coefficient retrieval (section 2.3) from unnecessary amplification of small-scale noise otherwise remaining in the retrieved transmissions.

[18] Regarding the reference heights, for frequencies sensitive to water vapor (channels near 22 and 183 GHz, highest ones up to 182.0 GHz), $z_{\text{ref}j}$ is typically set to 30 km, since transmission is essentially unity (or zero dB) at >25 km because absorption is already negligible at these heights. In the OPS $\mathcal{T}_j^{\text{log}}(a)$ is therefore set to zero dB above $z_{\text{ref}j}$ (foreclosing any potential problems with residual noise in subsequent uses of $\mathcal{T}_j(a)$ at these “heights beyond”). For ozone-sensitive frequencies (195 GHz line), $z_{\text{ref}j}$ is typically set to 50 km.

[19] This normalization is at the same time the key step of self-calibration of LMO amplitude measurements: as long as the transmitted signals are stable over the duration of the occultation event from height z_{ref} downward (i.e., over about 30 s for LMO), each individual profile is a reliable measure of the atmospheric absorption at frequency j at a given

location and time and independent from any measurements before, at the same time, or after. A small constant residual of transmissions at the reference height does not matter since the absorption coefficients derived from transmissions only depend on the derivative $d \ln \mathcal{T}_j(a)/da$ (see section 2.3).

[20] As a final step of transmission retrieval we compute differential (log-)transmission profiles between neighbor frequency pairs f_j and f_k [Kursinski et al., 2002; Gorbunov and Kirchengast, 2005],

$$\mathcal{T}_{jk}^{\log}(a) = \mathcal{T}_k^{\log}(a) - \mathcal{T}_j^{\log}(a) [\text{dB}], \text{ with } k = j + 1, \quad (4)$$

where the resulting $\mathcal{T}_{jk}^{\log}(a)$ [dB] profile is allocated to frequency channel j and can also be reconverted to the dimensionless $\mathcal{T}_{jk}(a)$ as needed. Thus, using for example a five frequency setup (as in the baseline case of the performance analysis in section 4), we will obtain four differential transmission profiles; that is, the number of differential transmission profiles is always one less than the number of direct transmission profiles. Nevertheless, the algorithms for the subsequent absorption coefficient and atmospheric profile retrievals are identical for using either $\mathcal{T}_{jk}(a)$ or $\mathcal{T}_j(a)$ as input (except that one profile less is fed in if using differential transmissions). For convenience we therefore use hereafter in equations only $\mathcal{T}_j(a)$, with the understanding this always coexpresses $\mathcal{T}_{jk}(a)$, and analogously we proceed for differential absorption coefficients. In the respective descriptions we indicate this by including the optional word “(differential)” as adjective to transmission/absorption coefficient.

[21] Practically we use differential transmissions as the primary mode of processing (leaving use of direct transmissions as a secondary option), since using differential transmissions cancels unwanted broadband effects common to the direct transmissions and particularly also amplitude scintillations from atmospheric turbulence to a high degree [Kursinski et al., 2002; Gorbunov and Kirchengast, 2007; Kursinski et al., 2009]. Detailed wave-optics-based results on the high quality of differential transmissions when dealing with scintillating LMO signals were reported by Gorbunov and Kirchengast [2005, 2007].

2.3. Absorption Coefficient Retrieval

[22] The profiles of (differential) absorption coefficient as function of height z at each frequency channel j , $k_j(z)$, can be derived from the profiles of impact parameter a , (differential) transmission, $\mathcal{T}_j(a)$, and radial distance from Earth’s local center of curvature, $r(a) = a/n(a)$, where $n(a)$ is the refractive index profile. An “absorptive” Abel transform akin to the well known “refractive” Abel transform of GRO [Fjeldbo et al., 1971] is used for this purpose. Following Kursinski et al. [2002], it reads,

$$k_j(z_i) = \frac{1}{\pi} \frac{da}{dr} \Big|_{a=a_i} \int_{a_i}^{a_i^{\text{top}}} \frac{d \ln \mathcal{T}_j(a)}{da} \frac{1}{\sqrt{a^2 - a_i^2}} da, \quad (5)$$

where all needed input profiles are available from the previous transmission and refractivity retrievals (where also levels z_i have been obtained as $z_i = r_i(a_i) - \text{Earth’s local}$

radius of curvature). In the OPS we use an equivalent but numerically more robust alternative formulation with differentiation past the integration [Gorbunov et al., 2007], leading to somewhat less amplification of noise (an amplification intrinsic to absorptive Abel transforms [e.g., Sofieva and Kyrölä, 2004]), which reads,

$$A\{a \cdot \ln \mathcal{T}_j(a)\}_i = \int_{a_i}^{a_i^{\text{top}}} a \cdot \ln \mathcal{T}_j(a) \frac{1}{\sqrt{a^2 - a_i^2}} da, \quad (6)$$

$$k_j(z_i) = \frac{1}{\pi} \frac{1}{a_i} \frac{d}{dr} \left(A\{a \cdot \ln \mathcal{T}_j(a)\}_i \right), \quad (7)$$

where likewise all needed input is available from the previous processing steps. The upper limit a_i^{top} of the Abelian integral $A\{\dots\}$, which is theoretically at infinite height, is set to correspond to a height $z_{\text{ref}j} + \Delta z/2$ since log-transmissions (optical thicknesses) beyond are zero anyway (see section 2.2) which is why they yield no contribution to the integral.

[23] In the OPS we again smooth at this step by applying a moving third-order polynomial filter to $\mathcal{T}_j(a)$ and $A\{a \cdot \ln \mathcal{T}_j(a)\}$ before their use in equation (6) resp. equation (7), with the width of the filtering polynomial set to about 1 km. This prevents the subsequent atmospheric profiles retrieval from unnecessary small-scale noise otherwise remaining in the retrieved (differential) absorption coefficient profiles.

2.4. Atmospheric Profiles Retrieval

[24] Using the profiles of refractivity $N(z)$ and (differential) absorption coefficients $k_j(z)$, we retrieve atmospheric profiles of pressure $p(z)$, temperature $T(z)$, water vapor pressure $e(z)$, cloud liquid water density $\rho_{\text{lw}}(z)$, and optionally ozone volume mixing ratio $V_{\text{O}_3}(z)$. We do this level-by-level top downward via optimal estimation constrained by a set of physical equations relating these state variables to $N(z)$ and $k_j(z)$ as well as $p(z)$, $T(z)$, and $e(z)$ to each other and specific humidity $q(z)$, which is cocomputed in this estimation. This level-by-level approach effectively avoids potential numerical problems from an otherwise large system of nonlinear equations, since only a small limited system needs to be solved at each level. We also derive profiles of air density and of geopotential height of pressure levels with standard formulae [e.g., Salby, 1996] from the retrieved variables in postprocessing (not further addressed here).

[25] The equations used to connect the atmospheric state to $N(z)$ and $k_j(z)$ are, in forward model (FM) form, the following. The first is the refractivity equation after Smith and Weintraub [1953] [see also, e.g., Kursinski et al., 1997],

$$N^{\text{FM}}(z) = 77.60 \frac{p(z)}{T(z)} + 3.73 \cdot 10^5 \frac{e(z)}{T(z)^2}, \quad (8)$$

with p and e in units of hPa and T in units of K yielding N^{FM} in units of N (N-units). The other ones are the absorption coefficient equations embodied in an advanced version of Liebe’s spectroscopic model of microwave complex

refractivity (Millimeter Wave Propagation Model MPM93 [Liebe, 1989; Liebe *et al.*, 1993]),

$$k_j^{\text{FM}}(z) = 10^{-3} \cdot \frac{4\pi\nu_j}{c} \cdot \text{Im}(N_C^{\text{FM}}(\nu_j, p(z), T(z), e(z), V_{\text{O}_3}(z), \rho_{\text{lw}}(z), \rho_{\text{iw}}(z), R_r(z))), \quad (9)$$

where $\text{Im}(N_C^{\text{FM}}(\cdot))$ provides the imaginary part of refractivity in units of N (N-units), $c = 299\,792\,458 \text{ m s}^{-1}$ is the speed of light, ν_j is the frequency in [Hz], and k_j^{FM} is obtained in units of km^{-1} . As seen in equation (9) the advanced MPM93 model $N_C^{\text{FM}}(\cdot)$ accounts also for the effects of ice water density $\rho_{\text{iw}}(z)$ and rain rate $R_r(z)$ on $k_j(z)$, in addition to those from the state variables of retrieval interest. Modeling the full complex refractivity, it also accounts, on top of $N(z)$ according to equation (8), for the very small nondispersive effects on the real part of refractivity (which are negligible in the application context here). The main updates of the advanced MPM93 in the EGOPS software relative to Liebe's original MPM93 include (besides transfer to Fortran 95/double precision): nondispersive refractivity consistent with equation (8), 195 GHz ozone line added following Herman *et al.* [2003], and rain rate performance improved based on data from Olsen *et al.* [1978].

[26] For providing the inverse connection on the sensitivity of $N(z)$ and $k_j(z)$ to the state variables, as well needed in the optimal estimation process [e.g., Rodgers, 2000], we use the adjoint model (AM) of the tangent-linear of the advanced MPM93 model, $\mathbf{K}_C^{\text{AM}}(\cdot)$, to obtain the respective Jacobian matrices,

$$\mathbf{K}^{N,\text{AM}}(z) = \text{Re}(\mathbf{K}_C^{\text{AM}}(\nu_j, p(z), T(z), e(z), V_{\text{O}_3}(z), \rho_{\text{lw}}(z), \rho_{\text{iw}}(z), R_r(z))), \quad (10)$$

$$\mathbf{K}_j^{k,\text{AM}}(z) = 10^{-3} \cdot \frac{4\pi\nu_j}{c} \cdot \text{Im}(\mathbf{K}_C^{\text{AM}}(\nu_j, p(z), T(z), e(z), V_{\text{O}_3}(z), \rho_{\text{lw}}(z), \rho_{\text{iw}}(z), R_r(z))), \quad (11)$$

where

$$\mathbf{K}^{N,\text{AM}}(z) = \left(\frac{\partial N}{\partial T}(z), \frac{\partial N}{\partial e}(z), \frac{\partial N}{\partial \rho_{\text{lw}}}(z), \dots \right)^{\text{T}}, \quad (12)$$

$$\mathbf{K}_j^{k,\text{AM}}(z) = \left(\frac{\partial k_j}{\partial T}(z), \frac{\partial k_j}{\partial e}(z), \frac{\partial k_j}{\partial \rho_{\text{lw}}}(z), \dots \right)^{\text{T}}, \quad (13)$$

which are applied level-by-level as seen further below. We restricted to explicitly show those sensitivity elements only in equations (12) and (13), which we use hereafter in explaining the estimation process and in the performance analysis in sections 3 to 4. That is, if we, for example, have frequency channels at the 195 GHz ozone line included and coretrieve ozone volume mixing ratio $V_{\text{O}_3}(z)$, we also will exploit the sensitivities $\partial N/\partial V_{\text{O}_3}$ and $\partial k_j/\partial V_{\text{O}_3}$. More generally speaking, every relation and sensitivity between $N(z)$, $k_j(z)$, and the state variables that is provided by equations (8)

to (11), or by any future update to these formulations, can readily be included into the chosen FM-AM approach, making it very versatile.

[27] Technically, the source code of the adjoint model $\mathbf{K}_C^{\text{AM}}(\cdot)$ was automatically generated from the source code of the forward model $N_C^{\text{FM}}(\cdot)$ using the Tangent-Linear and Adjoint Model Compiler [Giering and Kaminski, 1998], with minor postediting needed. The Jacobians (sensitivity elements) are accurate for any given state $(p, T, e, \rho_{\text{lw}}, \dots)$ because of local linearity of the model in the neighborhood of a given state, even though $N_C^{\text{FM}}(\cdot)$ is not linear if viewed over its complete relevant state-space. When working with differential transmissions, the differencing between the appropriate frequency pairs is also performed for the modeled absorption coefficients (equation (9)) and Jacobians (equation (13)) so that they correctly match the retrieved differential absorption coefficients in this case.

[28] The additional physical equation used to constrain the inversion is the hydrostatic equation with the equation of state in moist air embedded [e.g., Salby, 1996],

$$\frac{d \ln p(z)}{dz} = -\frac{g(z)}{R_d T_v(z)}, \quad (14)$$

where g is the acceleration of gravity (formulated according to a standard $g(z, \text{latitude})$ model), $R_d = 287.06 \text{ J kg}^{-1} \text{ K}^{-1}$ is the gas constant of dry air, and $T_v(z)$ is the virtual temperature. The latter is, together with specific humidity $q(z)$, included according to common formulations [e.g., Salby, 1996],

$$T_v(z) = T(z) \cdot (1 + c_w \cdot q(z)), \quad (15)$$

$$q(z) = a_w \cdot \frac{e(z)}{(p(z) - b_w \cdot e(z))}, \quad (16)$$

where $a_w = R_d/R_w (\cong 0.622)$ is the dry/water ratio of gas constants with $R_w = 461.52 \text{ J kg}^{-1} \text{ K}^{-1}$ the water vapor gas constant, and $b_w = 1 - a_w (\cong 0.378)$ and $c_w = 1/a_w - 1 (\cong 0.6077)$ are standard moist-air constants.

[29] Using equations (8) to (16) we implemented the retrieval algorithm in the OPS as illustrated in Figure 3, where ρ_{lw} is for simplicity denoted lw and q is not separately highlighted within the process since being a dependent coestimate $q(e, p)$ only (see equation (16)). Also optional variables (V_{O_3}, \dots) are not shown for conciseness (without loss of generality they are represented by lw) and since not needed in sections 3 to 4. Overall, the retrieval of the atmospheric state (p, T, e, lw) from (N, k_j) at each height is obtained by downward integration of the hydrostatic equation (equation (14)), which first yields p . Subsequently, $T, e,$ and lw are obtained by computing a best-linear unbiased estimate (BLUE) of them given (p, N, k_j) .

[30] More specifically, equation (14) is integrated top down starting from an initial height z_{Top} (75 km in OPS) with an initial state $(p_{\text{Top}}, T_{\text{Top}}, e_{\text{Top}} = lw_{\text{Top}} = 0)$, which can be of coarse accuracy as any initialization errors decay quickly within the first three scale heights, i.e., essentially within the mesosphere (in the OPS p_{Top} and T_{Top} are currently estimated from the local scale height about z_{Top} , obtained from $N(z)$, proportional to air density, and the

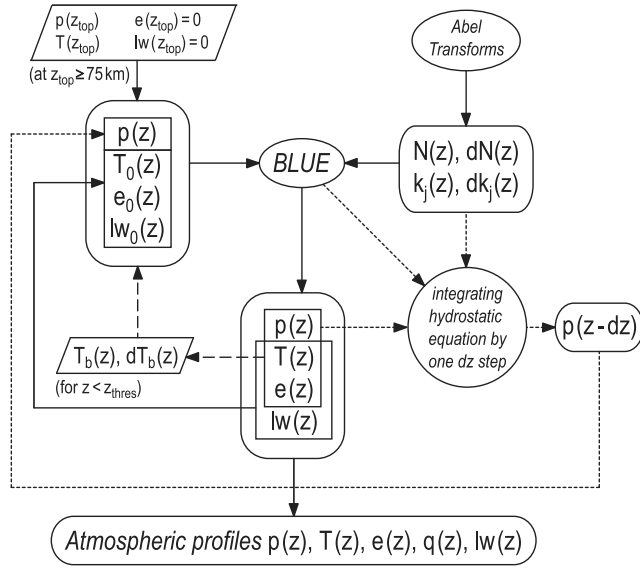


Figure 3. Overview on the retrieval of atmospheric profiles from LMO data as applied in EGOPS5.

local equation of state). In order to ensure accurate values $p_i = p(z_i)$ at each next downward height level z_i , a fourth-order Runge-Kutta integration [e.g., *Gershenfeld, 1999*] is used over each integration step, which itself is set reasonably small (100 m in OPS). This integration involves already the BLUE algorithm summarized below, in order to obtain, for the needed Runge-Kutta substeps, T_v (equation (15)) based on T and e estimated from (p, N, k_j) at the substep levels.

[31] After each integration step yielding p_i at height z_i , the BLUE algorithm is applied at z_i and estimates the state (T_i, e_i, lw_i) from the pressure and observational constraint at z_i $(p_i, N_i, k_{j,i})$, where the pressure p_i acts as a “backbone” for this local state estimation (ensuring it to be numerically very robust) and where the state at the previous height $(T_{i+1}, e_{i+1}, lw_{i+1})$ is used as first guess (ensuring very fast convergence). Practically, the contributions of e and lw are negligible in (N, k_j) at higher altitudes at LMO frequencies, wherefore e is coestimated with p and T only below 24.5 km and lw in addition only below 8.5 km. Also it can occur at lower-to-middle tropospheric heights below about 3 to 7 km in adverse conditions (strongly damped and/or strongly scintillating amplitudes) that some limited prior information is useful, which is accommodated for by an option for prior temperature information below a height $z_{\text{thres}} < 7$ km, as discussed further below. The specific formulation of the BLUE in the OPS, founded on the basic atmospheric profiles retrieval algorithm of *Gorbunov et al. [2007]*, is an iterative Gauss-Newton optimal estimator [*Rodgers, 2000*] implemented as follows,

$$\mathbf{x}_{n+1} = \mathbf{x}_n + \left(\mathbf{K}_n^T \cdot \mathbf{C}_y^{-1} \cdot \mathbf{K}_n + \mathbf{C}_b^{-1} \right)^{-1} \cdot \left[\mathbf{K}_n^T \cdot \mathbf{C}_y^{-1} (\mathbf{y} - \mathbf{y}^{\text{FM}}(\mathbf{x}_n)) - \mathbf{C}_b^{-1} (\mathbf{x}_n - \mathbf{x}_b) \right], \quad (17)$$

$$\mathbf{y} = (N, k_j)^T, \mathbf{y}^{\text{FM}} = (N^{\text{FM}}, k_j^{\text{FM}})^T, \quad (18)$$

$$\mathbf{C}_y = \text{Diag}(\sigma_N^2, \sigma_{k_j}^2), \quad (19)$$

$$\sigma_N = \begin{cases} N \cdot \text{Min} \left[f_{\text{stratbot}} \cdot \exp\left(\frac{(z - z_{\text{stratbot}})}{H_{\text{strat}}}\right), f_{\text{max}} \right] & \text{for } z \geq z_{\text{stratbot}} \\ N \cdot \left[f_{\text{stratbot}} + f_0 \left(\frac{1}{\text{Max}(z, 1\text{km})} - \frac{1}{z_{\text{stratbot}}} \right) \right] & \text{for } z < z_{\text{stratbot}} \end{cases}, \quad (20)$$

$$\sigma_{k_j} = f_w \cdot \sigma_{k_j}^{\text{ref},j} \cdot \left(\frac{1}{\text{Max}(T_j(z), 10^{-6})} + \frac{1}{W_2} \right) \cdot f_{T_b}, \quad (21)$$

$$f_{T_b} = \begin{cases} 1 & \text{for } z \geq z_{\text{thres}} \\ \text{Min} \left[f_T^{z_{\text{thres}}} + \left(\frac{df_T}{dz} \right) (z_{\text{thres}} - z), f_T^{\text{max}} \right] & \text{for } z < z_{\text{thres}} \end{cases}, \quad (22)$$

$$\mathbf{K} = \left(\mathbf{K}^{N,AM}, \mathbf{K}_j^{k,AM} \right)^T, \quad (23)$$

$$\mathbf{x} = (T, e, lw)^T, \mathbf{x}_0 = (T_{\text{init}}, e_{i+1}, lw_{i+1})^T, \mathbf{x}_b = \mathbf{x}_0, \quad (24)$$

$$T_{\text{init}} = \begin{cases} T_{i+1} & \text{for } z \geq z_{\text{thres}} \\ T_b & \text{for } z < z_{\text{thres}} \end{cases}, \quad (25)$$

$$\mathbf{C}_b = \text{Diag}(\sigma_T^2, \sigma_e^2, \sigma_{lw}^2), \quad (26)$$

$$\sigma_T = \begin{cases} s_T^{\text{large-const}} & \text{for } z \geq z_{\text{thres}} \\ \text{Min} \left[s_T^{z_{\text{thres}}} + \left(\frac{ds_T}{dz} \right) (z_{\text{thres}} - z), s_T^{\text{max}} \right] & \text{for } z < z_{\text{thres}} \end{cases},$$

$$\sigma_e = s_e^{\text{large-const}}, \sigma_{lw} = s_{lw}^{\text{large-const}}, \quad (27)$$

where the symbols and definitions include

- n the iteration index of the iterative optimal estimator ($n = 0, \dots, \text{Min}[n_{\text{converged}}, 12]$);
- \mathbf{y} the measurement vector consisting of retrieved refractivity N and (differential) absorption coefficients k_j ;
- \mathbf{y}^{FM} the forward modeled measurement vector updated at each iteration step using equations (8) and (9);
- \mathbf{C}_y the measurement error covariance matrix, set as diagonal matrix;
- σ_N the standard error of refractivity modeled following *Steiner and Kirchengast [2005]* and *Steiner et al. [2006]*, with settings bottom height of stratosphere $z_{\text{stratbot}} = 15$ km, fractional error there $f_{\text{stratbot}} = 0.001$, tropospheric bottom fractional error $f_0 = 0.01$, stratospheric error scale height $H_{\text{strat}} = 50$ km, and maximum fractional error $f_{\text{max}} = 0.2$ for this study (based on approximating estimated refractivity errors);

- σ_{k_j} the standard error of the (differential) absorption coefficients k_j ;
- $\sigma_{k_j}^{z_{\text{ref}j}}$ the standard error of k_j estimated within the height range $z_{\text{ref}j}$ to $z_{\text{ref}j} - \Delta z$ (for comparison, see equation (2));
- $T_f(z)$ the transmission profile in units of W W^{-1} (i.e., unity at $z_{\text{ref}j}$) providing the height-dependent error weighting (the smaller one of the two direct transmissions used at each height level in case of differential retrieval);
- W_2 a 2nd error-weighting option currently unused and set to unity;
- f_w a scalar weighting factor with baseline setting 0.5 (used in this study, yielding $\sigma_{k_j} = \sigma_{k_j}^{z_{\text{ref}j}}$ at $z_{\text{ref}j}$);
- f_{T_b} an error amplification factor downweighting the influence of the k_j 's relative to N below z_{thres} , with settings $f_{T_b}^{z_{\text{thres}}} = 5$, $(df_{T_b}/dz) = 2.5 \text{ km}^{-1}$, $f_{T_b}^{\text{max}} = 10$ used in this study;
- K** the Jacobian weighting matrix defined in equations (10) and (11), updated at each iteration step n ;
- x** the state vector to be estimated, updated at each iteration step n (until convergence);
- \mathbf{x}_0 the initial guess set for **x**, with T_{init} set to the background (prior) temperature T_b below z_{thres} ;
- \mathbf{x}_b the background (a priori) state set identical to the initial guess state;
- C_b** the background (a priori) error covariance matrix, set as diagonal matrix;
- σ_T the adopted standard error of T_{init} set to a large constant ($s_T^{\text{large-const}} = 100 \text{ K}$) above z_{thres} and to the error estimate for T_b below z_{thres} (settings $s_T^{z_{\text{thres}}} = 0.75 \text{ K}$, $(ds_T/dz) = 0.15 \text{ K km}^{-1}$, $s_T^{\text{max}} = 1.5 \text{ K}$ in this study);
- σ_e and σ_{lw} the adopted standard errors of e_{i+1} and lw_{i+1} , respectively, both set to large constants ($s_e^{\text{large-const}} = 25 \text{ hPa}$ resp. $s_{lw}^{\text{large-const}} = 5 \text{ g m}^{-3}$).

[32] How we assign the variances in **C_b** makes the utility of the a priori term $\mathbf{C}_b^{-1}(\mathbf{x}_n - \mathbf{x}_b)$ in equation (17) clear: its influence is made negligible above z_{thres} , where the retrieval scheme is therefore independent of prior information, and it inserts the background temperature constraint below z_{thres} if z_{thres} comes to be set to a height above the bottom level of **x**. In the OPS a nonzero z_{thres} up to a height of 7 km, is automatically set if a cloud top is detected (where clouds below strongly damp the amplitudes) or if a “scintillation top” is detected (where scintillations below strongly disturb the amplitudes). For cloud top detection we use a “trial retrieval” intentionally disabling coretrieval of lw within (T_i, e_i, lw_i) , which in case of significant lw amount starts to produce a strongly distorted retrieved T profile at cloud top used to assign z_{thres} . For scintillation-top detection we estimate the RMS amplitude fluctuation at the subkilometer scale from $A_j(a)$ (section 2.2) at the lowest frequency (typically within 8 to 18 GHz) and assign z_{thres} to a level where an RMS threshold empirically determined from simulation studies starts to be exceeded and stays exceeded over the entire profile below (threshold 0.1 dB for 1-km-averaged 10-Hz-sampling-rate RMS estimates at 10 GHz, linearly scaled with frequency; if coretrieval of lw , restriction to

maximum scintillation top of 3 km from experience). This scintillation-top detection is the current approach designed for geometric optics retrieval (as applied in this study); ongoing work including wave optics retrieval is likely to eliminate this specific approach.

[33] Furthermore, if the lowest frequency is $>15 \text{ GHz}$ we set z_{thres} to a minimum of 3 km, since amplitudes of channels that close to the 22 GHz water vapor line center will generally be strongly damped already in the lowest 3 km. Practically the z_{thres} setting, the highest z_{thres} from the criteria above finally adopted if nonzero, plays a role in the lower troposphere. In the performance analysis of section 4, where we focus on the upper troposphere/lower stratosphere (UTLS) above 5 km (channels $> 15 \text{ GHz}$ only), it is of minor relevance given the z_{thres} upper limit of 7 km. If the lower troposphere is targeted in addition, extension by channels with weak absorption at frequencies $<15 \text{ GHz}$ is promising to enable reaching down to the boundary layer without z_{thres} [e.g., *Kursinski et al.*, 2002; *Gorbunov and Kirchengast*, 2005].

[34] The BLUE needs at least three pieces of information in (N, k_j) to form a determined system of equations for retrieving the state (T, e, lw) . Thus at least three LMO channels (leading to refractivity plus two differential absorption coefficient profiles) is the typical minimum LMO mission design [e.g., *Kirchengast and Hoeg*, 2004]; further channels improve robustness and can be used to extend the humidity height range (as section 4 shows for adding two 183 GHz line channels) or to coretrieve additional variables (as noted above for ozone if adding 195 GHz line channels; see also *Kursinski et al.* [2009], who suggest to coretrieve also cloud temperature). If in the lower troposphere toward or in the boundary layer part of the absorption information is lost due to strong damping/fluctuations in adverse (e.g., moist tropical) conditions, it is the prior information below z_{thres} that retains robust retrieval. We found temperature the most suitable, and at the same time fully sufficient, minimal background information in this case since it is well predictable and accurate in the (lower) troposphere in modern weather prediction and analysis systems, especially at (moist) low latitudes where adverse LMO signal conditions may mainly occur.

[35] In the OPS we ensure, in case of nonzero z_{thres} , an accurate choice of T_b for usage below z_{thres} (equation (25)) by selecting a temperature profile which best fits the already retrieved temperature profile within one scale height (8 km) above z_{thres} . The basis for the selection is a small ensemble (baseline 9) of trial profiles, which are extracted from a 24 h ECMWF forecast field with about 100 km horizontal resolution within a geographic area of a few degrees (baseline 2° to 3°) around the occultation event location. The trial profile which fits best to the retrieved T profile within a scale height above z_{thres} is then chosen as profile T_b . This profile T_b is found superior to the (already good) choice of just the colocated ECMWF forecast profile. This happens because the fit further mitigates any small potential background bias by selecting that profile from an ensemble of good candidate profiles which best matches the retrieved T profile above z_{thres} . The T_b error estimates as chosen for equation (27) are thus tentatively conservative.

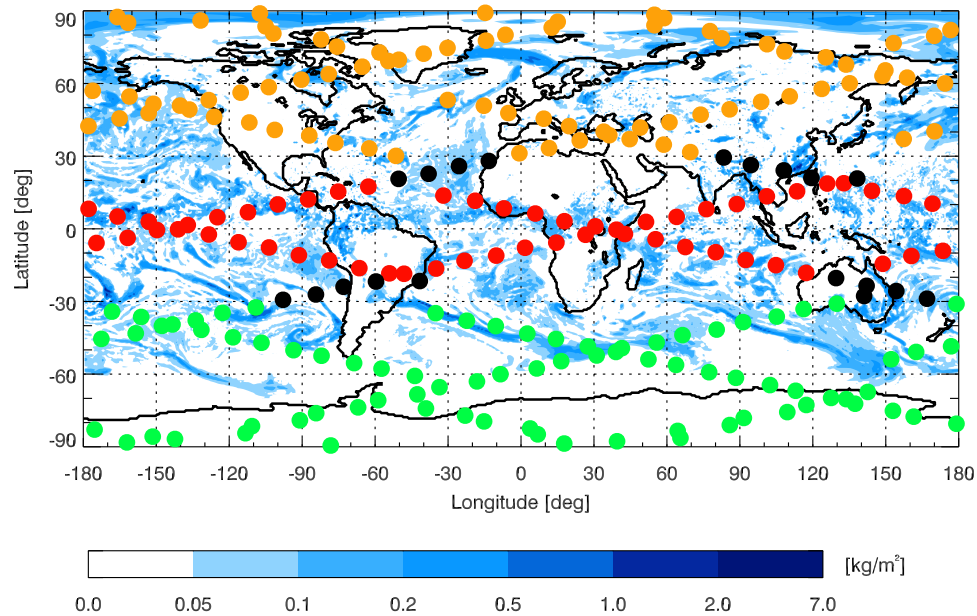


Figure 4. Coverage by LEO-LEO occultation events as used for the analysis. Events are marked as sorted into Southern Hemisphere extratropics (green, 90°S to 30°S), tropical (red, 20°S to 20°N), and Northern Hemisphere extratropics (orange, 30°N to 90°N), with the subtropical events (20° to 30°) left black. The background shows vertically integrated liquid water content, indicating cloud coverage, of the ECMWF T511L91 analysis used (15 July 2006, 12 UTC).

[36] Wave-optics-type processing (Canonical Transform [Gorbunov, 2002; Gorbunov and Lauritsen, 2004], Full Spectrum Inversion [Jensen et al., 2003], and Phase Matching [Jensen et al., 2004]) combined with a differential transmission approach can reduce scintillations already during transmission retrieval. Thus downweighting of absorption coefficients in the BLUE algorithm may be avoided. As shown by Gorbunov and Kirchengast [2005, 2007], especially the use of differential transmission profiles based on canonically transformed amplitudes is promising to enable accurate retrieval of atmospheric profiles without prior information even in the case of severe turbulence. This means that when the geometric optics algorithm introduced here is combined with wave optics bending angle and differential transmission retrieval in future applications, z_{thres} may in general be invoked close to the boundary layer only, where the signal-to-noise ratio is very small due to strong absorption anyway.

3. Performance Analysis Design

[37] For assessing the performance of the retrieval algorithm described above and implemented in the OPS part of the EGOPS5 software introduced in section 2.1, we carried out forward modeling and related observation system error modeling as well as retrieval processing using EGOPS5 in an end-to-end manner, enabling quasi-realistic simulations.

[38] The end-to-end simulations were performed for two different sets of frequencies, one set containing three frequencies around the 22 GHz water vapor absorption line only (“22 GHz case,” including 17.25 GHz, 20.2 GHz, 22.6 GHz), and the other one containing two additional frequencies near the 183 GHz absorption line (“22 + 183 GHz case,” including also 179 GHz and 182 GHz). All

adopted frequencies are compliant with international (World Radio Conference) frequency regulations, which in particular forbid use of frequencies directly around line center for active sounding (e.g., 182 GHz is the closest possible to the 183.31 GHz line center). The atmospheric profiles retrieval performance resulting from these two cases is investigated.

[39] In particular, we assess the accuracy of pressure, temperature, and humidity profiles in the upper troposphere/lower stratosphere region (UTLS, 5 to 35 km) in four different large-scale regions, global 90°S to 90°N (GLO), tropics 20°S to 20°N (TRO), Northern Hemisphere extratropics 30°N to 90°N (NHE), and Southern Hemisphere extratropics 90°S to 30°S (SHE). If these atmospheric retrieval results fulfill observational requirements of an LMO mission design [e.g., Larsen et al., 2009], it is implicitly clear that also raw and intermediate profiles (e.g., amplitudes, transmissions, absorption coefficients) are of adequate quality [Kirchengast et al., 2004]. To gain insight into the full retrieval chain it is of interest to inspect also these intermediate profiles. We thus discuss exemplary amplitude, transmission, and absorption coefficient profiles since these are new compared to the excess phase, bending angle, and refractivity profiles well known from GRO (see sections 1 and 2.1).

[40] Regarding the forward modeling, a full day of LMO measurements was simulated assuming two transmitter satellites at a height of 800 km and two counter-rotating receiver satellites at a height of 650 km, both Sun-synchronous orbits, being a representative baseline constellation of LMO mission designs [e.g., Kirchengast and Hoeg, 2004]. This yielded 233 occultation events, illustrated in Figure 4, which are regularly distributed over the Earth (in a certain pattern that fills up to even coverage within several days) and where the coloring of events highlights the parti-

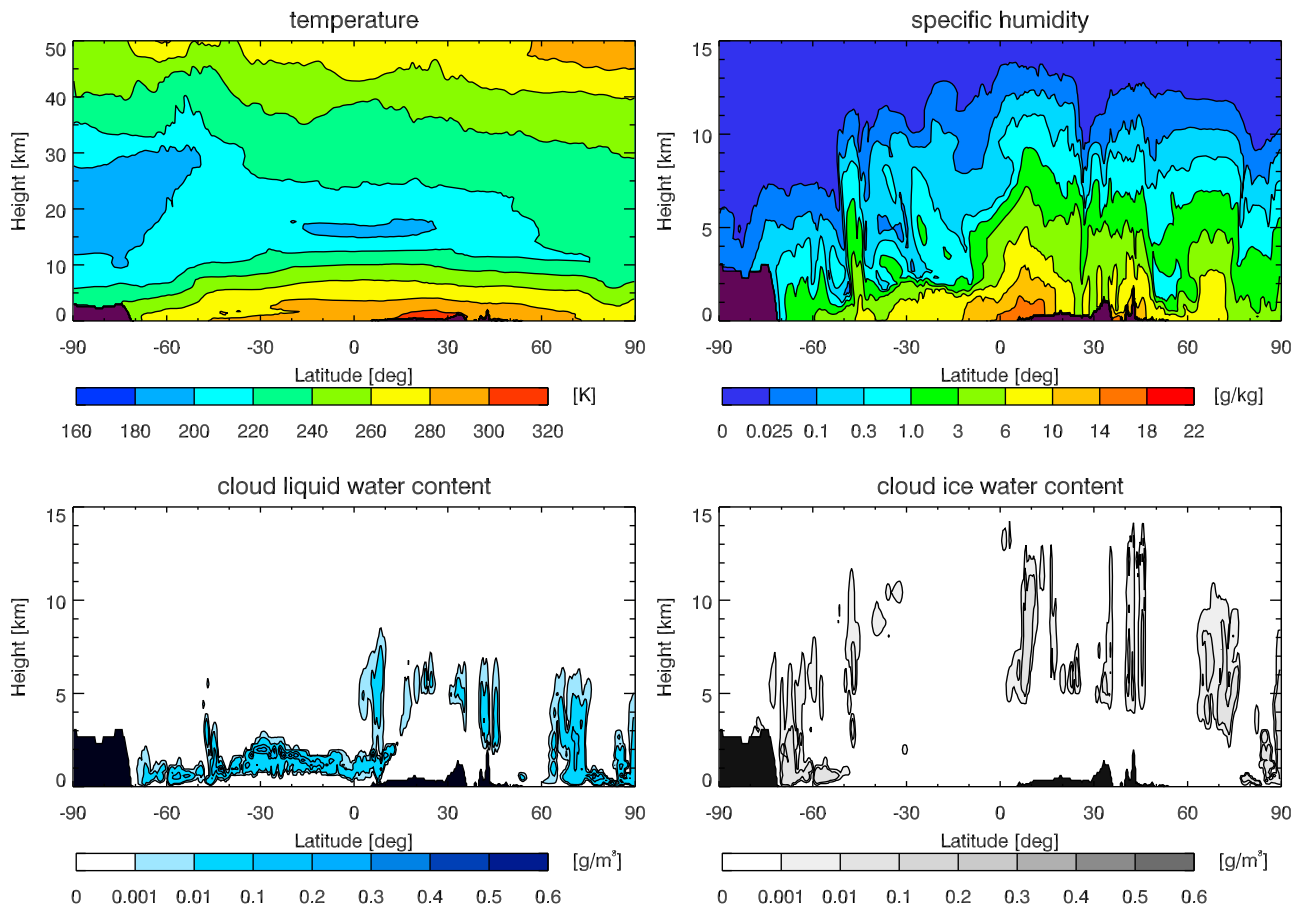


Figure 5. Latitude-versus-height cross sections of (top left) temperature, (top right) specific humidity, (bottom left) liquid water density, and (bottom right) ice water density at 0° longitude through the ECMWF analysis used in the simulations, indicating the atmospheric variability covered.

tioning into the TRO, NHE, and SHE regions. Realistic atmospheric fields were supplied by an ECMWF T511L91 analysis (horizontal resolution of about 40×40 km, 91 vertical levels from surface to 0.01 hPa) of 15 July 2006, 12 UTC (an arbitrary Northern Hemisphere summer/Southern Hemisphere winter day), including three-dimensional fields of liquid water and ice water in addition to supplying the basic fields of pressure, temperature, and humidity. In order to provide some insight to the variability in this analysis, Figure 4 illustrates the cloudiness as a backdrop to the LMO occultation event distribution and Figure 5 shows representative latitude-versus-height cross sections, indicating that events occur in a range of different conditions from dry to moist and clear to cloudy air.

[41] In simulating the excess phase and amplitude profiles of any single LMO event based on high-accuracy ray tracing and along-ray extinction integration at a 10 Hz sampling rate, we assumed local spherical symmetry around the atmospheric profiles, which we extracted from the ECMWF fields as vertical profiles at the occultation event location (retaining the liquid and ice clouds fully three-dimensional, however). In this way we disregard horizontal variations of the moisture and mass fields and related representativeness errors and enable quantification of observational and retrieval errors in pressure, temperature, and humidity without mixing in representativeness errors.

Keeping on the other hand liquid and ice water fields three-dimensional allows that the integration of cloud extinction along raypaths can still realistically account for the attenuation effects of these very inhomogeneous droplet and particle fields, for which any larger-scale symmetry approximation is invalid. The errors from horizontal variability in occultation-derived profiles were investigated, e.g., by *Foelsche and Kirchengast* [2004], *Syndergaard et al.* [2004], and *Schweitzer* [2004], where the latter work (using ECMWF T511L60 fields) found the RMS error of LMO humidity retrieval in the UTLS increased due to horizontal variability by up to about 4%, depending on the moisture content (the more water vapor the larger the influence). The contribution to LMO temperature retrieval RMS error was found <0.3 K in the UTLS as temperature reflects the generally smooth variability of the atmospheric mass field.

[42] Before being supplied as quasi-realistic observables to the retrieval system OPS, the forward modeled excess phase and amplitude profiles also get added errors due to atmospheric turbulence (superposed on log-amplitudes as white noise of strength consistent with the noise estimated in the wave-optics-based transmission retrieval performance work of *Gorbunov and Kirchengast* [2007]) as well as observation system errors. Regarding the latter, precise-orbit-determination (POD) errors and excess phase errors were modeled as in GRO simulations of *Steiner and*

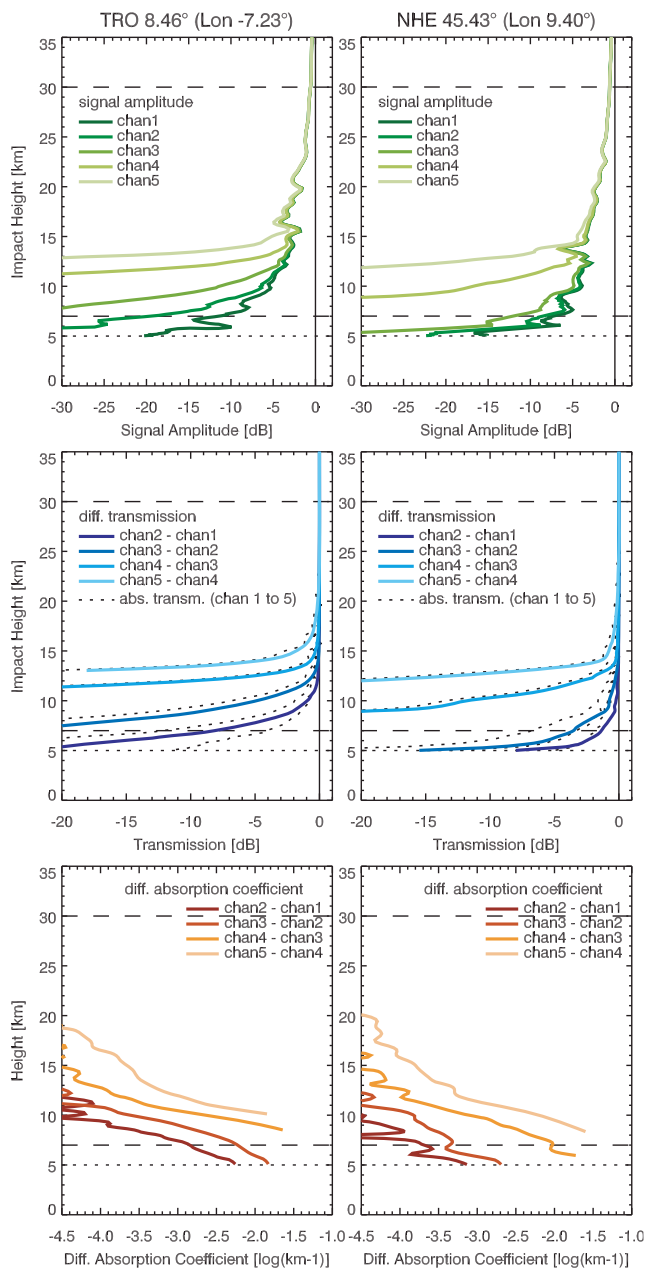


Figure 6. Examples for (top) LMO signal amplitudes (chan1 to chan5: 17.25 GHz, 20.2 GHz, 22.6 GHz, 179 GHz, 182 GHz), (middle) (differential) transmissions (heavy lines, differential transmissions; dotted lines, absolute transmissions), and (bottom) differential absorption coefficients. (left) A typical tropical occultation event. (right) A midlatitude summer event. Horizontal dotted/dashed lines depict target/threshold requirements concerning vertical domain for the ACCURATE concept targeting the UTLS region.

Kirchengast [2005] (without nonrelevant local multipath) and amplitude errors including thermal noise and drift errors as in LMO simulations by *Kirchengast et al.* [2004], reflecting the LMO design of *ESA* [2004a, 2004b]. In particular, amplitude thermal noise was modeled as white Gaussian noise based on a carrier-to-noise spectral density ratio (C/N_0) at the top of the atmosphere (TOA) of 67 dBHz (22 GHz channels) and 64 dBHz (183 GHz channels),

respectively. Amplitude drift was modeled as a linear drift with a standard slope of 0.06 dB min^{-1} (i.e., the slope for individual occultation events is generated as Gaussian random number using this slope as standard deviation), with the drift applied downward from the occultation event time corresponding to a reference height of 30 km. The technical feasibility of LMO instrumentation consistent with these specifications was investigated and established within technical studies of the *ESA* occultation mission concept *ACE+* [*ESA*, 2004b].

[43] Ionospheric effects were disregarded since related errors are negligible at the frequencies $>17 \text{ GHz}$ used here [e.g., *Gorbunov and Kirchengast*, 2005; *Kursinski et al.*, 2009], which are more than 10 times higher than for *GRO*.

[44] In the retrieval processing, based on the algorithmic chain described in section 2, we employed in addition to the standard bending angle and refractivity retrieval the differential transmission and absorption coefficient retrieval for supplying the needed inputs to the atmospheric profiles retrieval, which finally yielded pressure, temperature, and humidity profiles.

[45] The performance of the retrieved atmospheric profiles was then assessed by a statistical error analysis as follows: For each retrieved profile, the corresponding “true” collocated profile at the occultation event location from the *ECMWF* analysis used in the forward modeling was taken. Then difference profiles between these retrieved and “true” profiles were formed and profile ensembles gathered for the *GLO*, *TRO*, *NHE*, and *SHE* domains, for which sample mean difference (bias) profiles and sample standard deviation profiles were estimated using standard formulae [e.g., *Steiner and Kirchengast*, 2004]. Relative error quantities were obtained by dividing the absolute error quantities by the mean of all “true” profiles of an ensemble. Raw and intermediate profiles of the retrieval chain were inspected for preparing typical example cases, both for tropical and extratropical occultation events. The results are discussed in section 4.

4. Analysis Results and Discussion

[46] Figure 6 shows, for two occultation events representative of tropical and extratropical (midlatitude) conditions, amplitude profiles, (differential) transmission profiles, and (differential) absorption coefficient profiles for the five frequency channels simulated. All quantities are shown in logarithmic units since the relevant dynamic ranges of variation span about 3 orders of magnitude as a function of height.

[47] Amplitudes (Figure 6, top) are attenuated strongly from top downward, starting gradually as a damping of up to several dB by defocusing and then steepening as water vapor absorption becomes dominant, the more so the closer a channel is to the 22 GHz or 183 GHz line center and the more humid the atmospheric conditions are. The vertically integrated water vapor content is relatively high for both events, within 50 kg m^{-2} to 60 kg m^{-2} for the *TRO* event and within 30 kg m^{-2} to 40 kg m^{-2} in for the *NHE* event. Cloud liquid water is present as well (see the location of the events in Figure 4). Scintillation noise in the upper troposphere up to 10 to 15 km is not present in these geometric optics simulations to the degree it would be visible in

reality, or in wave optics simulations, on such amplitude profiles. The reason is that this noise was parameterized to match the correct (and smaller) differential transmission noise after wave optics processing [Gorbunov and Kirchengast, 2007] (see section 3). Defocusing features indicating the tropopause are well visible, e.g., at about 16 to 17 km for the TRO event. Attenuations >30 dB can no longer be reasonably exploited as signal-to-noise ratio (SNR) then approaches unity, which is why a range of channels is needed to cover the UTLS height range with adequate sensitivity.

[48] Differential transmissions (Figure 6, middle), available after the retrieval part described in section 2.2 and having defocusing and other broadband effects corrected, appear much smoother and highlight the dynamic range that is really available from absorption only, i.e., from that information which is actually exploitable in the subsequent retrieval. Transmissions from about -0.25 dB (95%) to -13 dB (5%) mark the best sensitivity range, and evidently the collection of four differential channels of the 22 + 183 GHz Case covers the heights up to about 18 km well with sensitivity. The two differential channels of the 22 GHz Case provide adequate sensitivity up to about 12 to 13 km only (and less if the upper troposphere is drier such as typically at high latitudes). As introduced by Kursinski *et al.* [2002, 2004] and Herman *et al.* [2004] based on more simplified climatological simulations, the channels near 183 GHz are thus needed for extending LMO water vapor sounding across the tropopause into the lower stratosphere. The absolute transmissions are shown as a backdrop to indicate, as a link from the top to the middle panels of Figure 6, that the background attenuation consumes additional dynamic range.

[49] Comparing the retrieved differential transmissions with the “true” ones computed during forward modeling we find that the RMS error is <0.2 dB ($<5\%$) from 5 to 7.5 km, <0.1 dB ($<2.5\%$) from 7.5 to 10 km, and clearly <0.05 dB ($<1\%$) above 10 km. These errors are consistent with those of Gorbunov and Kirchengast [2005, 2007] from more complex wave optics simulations processed down to the level of differential transmission profiles. While those wave optics simulations addressed 22 GHz channels only, the differential transmission of the close pair 179 GHz and 182 GHz is reasonably expected to show similar performance since there is no change in underlying physics. The “bridging” pair between 22.6 GHz and 179 GHz may leave in practice larger residuals, due to the large frequency spacing, though theoretically there is no spacing dependence given adequate wave optics retrieval [Gorbunov and Kirchengast, 2005]; this deserves additional future study. Compared to absolute transmissions, the errors in differential transmissions are as expected found significantly smaller (typically at least 4 times in our retrieval); in general the quantitative factor of improvement will depend on details of the transmission retrieval algorithm.

[50] Differential absorption coefficient profiles (Figure 6, bottom), available after the Abel transform step described in section 2.3, reflect in height the corresponding transmission sensitivity ranges but also indicate by their less smooth appearance the noise amplification (by a factor of about 2.4) inherent in this type of Abel transform from transmission toward local (at tangent point location) absorption coeffi-

cient profiles [Sofieva and Kyrölä, 2004]. Assuming for the sake of insight an effective optical path length of 300 km for the occultation rays (which was confirmed by ray-tracing simulations to be very suitable), the log-absorption coefficient “saturation limit” visible near 10^{-2} km^{-1} corresponds to about -15 dB (3%) transmission, the “noise limit” visible near 10^{-4} km^{-1} to about -0.15 dB (97%) transmission, respectively, neatly reflecting the sensitivity range available per channel as referred to above.

[51] Supplying this type of differential absorption coefficient profiles together with retrieved refractivity profiles (of the high performance well known from GRO [e.g., Steiner and Kirchengast, 2005]) to the atmospheric profiles retrieval (section 2.4), and producing the statistics, yields the performance analysis results for pressure, temperature, and humidity retrieval depicted in Figures 7 to 9. As introduced above we focus on the UTLS (5 to 35 km), since this is the core region of LMO design in the frame of the ACCURATE mission concept (section 1). For this concept the observational requirements, including on LMO temperature and humidity target and threshold height ranges and RMS accuracies within, have been specified by Larsen *et al.* [2009]. Figures 7 to 9 depict these requirements for context, where the pressure accuracy requirements have been set consistent with the temperature accuracy requirements, using GRO knowledge on error propagation [Rieder and Kirchengast, 2001; Steiner and Kirchengast, 2005].

[52] Figure 7 shows the statistical error estimates obtained for pressure, where the underlying atmospheric variability of pressure profiles in the global ensemble of the adopted ECMWF analysis field of 15 July (GLO, Figure 7, top left) derives mostly from the winter hemisphere (SHE, Figure 7, top right), which is sound. The global mean profile ranges from about 500 hPa at 5 km to about 6 hPa at 35 km and the error profiles are shown as percentages relative to this profile. The bias is very small at clearly $<0.1\%$ at all heights in all four regions, corresponding to a maximum uncertainty of about 5 m in altitude, or geopotential height, knowledge (0.1% pressure bias corresponds to about 7 m altitude error). There is a statistically significant positive bias visible in the lower stratosphere, though, likely indicating small imperfections in the initialization at high altitudes, which the hydrostatic integral carries downward. This was analyzed in detail for GRO [e.g., Rieder and Kirchengast, 2001; Gobiet and Kirchengast, 2004; Steiner and Kirchengast, 2005], and since pressure information is dominated by the refractivity information from excess phase, rather than the absorption coefficient information from amplitudes, the insights acquired with GRO apply also here. For real GRO data, residual biases $<0.15\%$ to 0.3% are achieved (altitude knowledge better than 10 m to 20 m [e.g., Kursinski *et al.*, 1997; Leroy, 1997]), and LMO biases a factor of 2 or so better appear sound.

[53] Pressure standard errors, and consequently total RMS errors given the very small biases, are found well within the target requirement of 0.2%, except in the SHE region above 30 km where this is slightly exceeded. Comparison of the 22 + 183 GHz Case (Figure 7, middle) and the 22 GHz Case (Figure 7, bottom) confirms that the pressure retrieval performance is essentially independent of the number of channels used, since governed by refraction information as

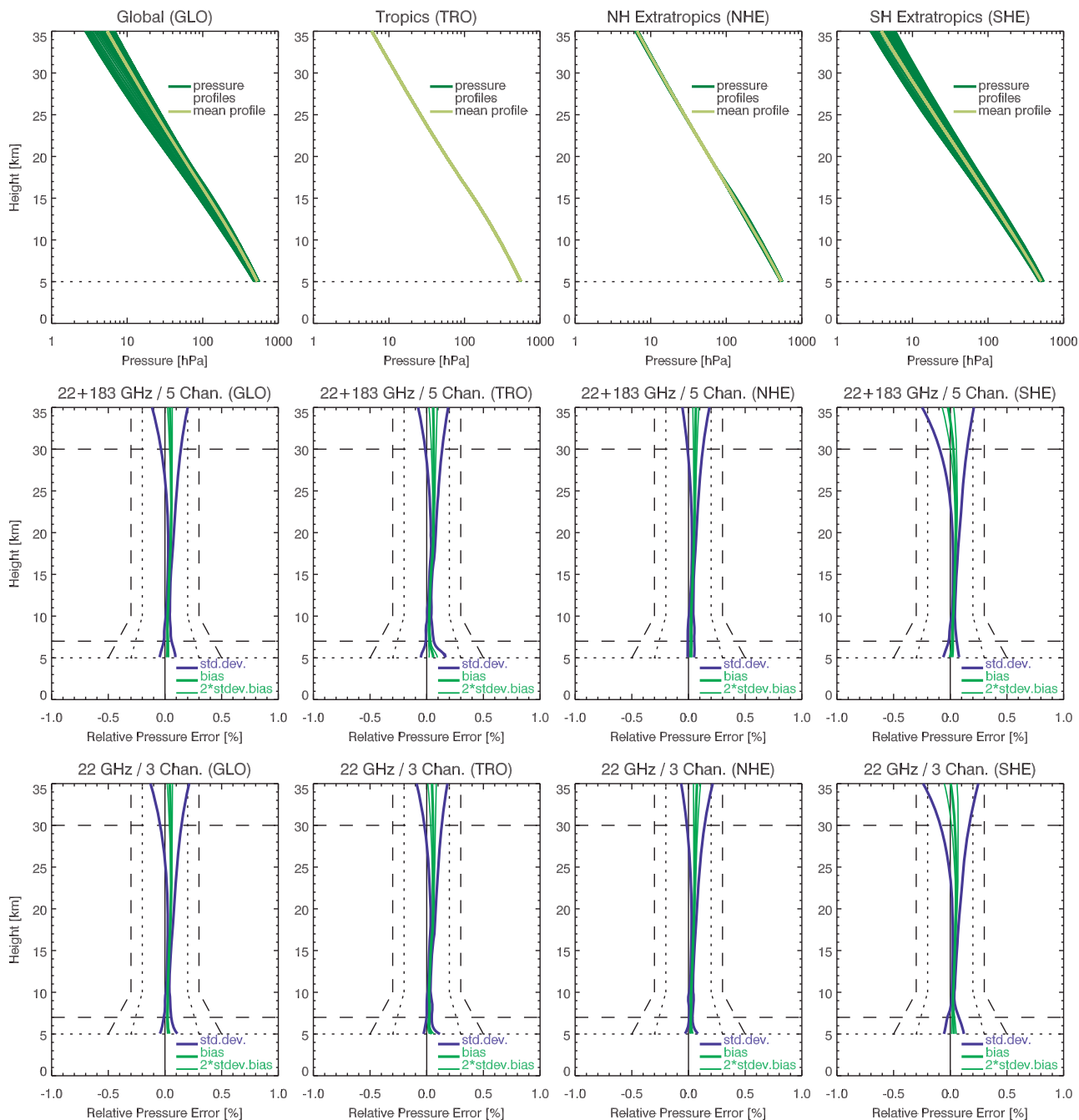


Figure 7. Pressure retrieval performance results in the four domains: (left) global (90°S to 90°N), (middle left) tropics (20°S to 20°N), (middle right) Northern Hemisphere extratropics (30°N to 90°N), and (right) Southern Hemisphere extratropics (90°S to 30°S). The second and third rows show the error estimates for the 22 + 183 GHz Case and the 22 GHz Case, respectively, where profiles of bias (heavy green) and, symmetrically about this, 2x standard deviation of the bias (thin green) and standard deviation (heavy blue, outer envelope profiles) are depicted. The dotted/dashed lines indicate target/threshold requirements for the ACCURATE concept (horizontal for height domain, vertical for RMS accuracy).

stated above, and the three frequencies near 22 GHz being sufficient to isolate pressure, temperature, and humidity below 8 to 12 km, where pressure deviates from the so-called dry pressure derived from refractivity [e.g., *Kursinski et al.*, 1997].

[54] Figure 8 shows the temperature retrieval performance results, where the ensembles of temperature profiles (Figure 8,

top) well represent both the stable tropical thermal structure with its marked tropopause (Figure 8, TRO panel) and the extratropical variability at middle and high latitudes (Figure 8, NHE, SHE panels), especially the marked winter variability including the very cold southern polar vortex profiles (Figure 8, SHE panel). The temperature retrievals (Figure 8, middle and bottom) are essentially unbiased and their stan-

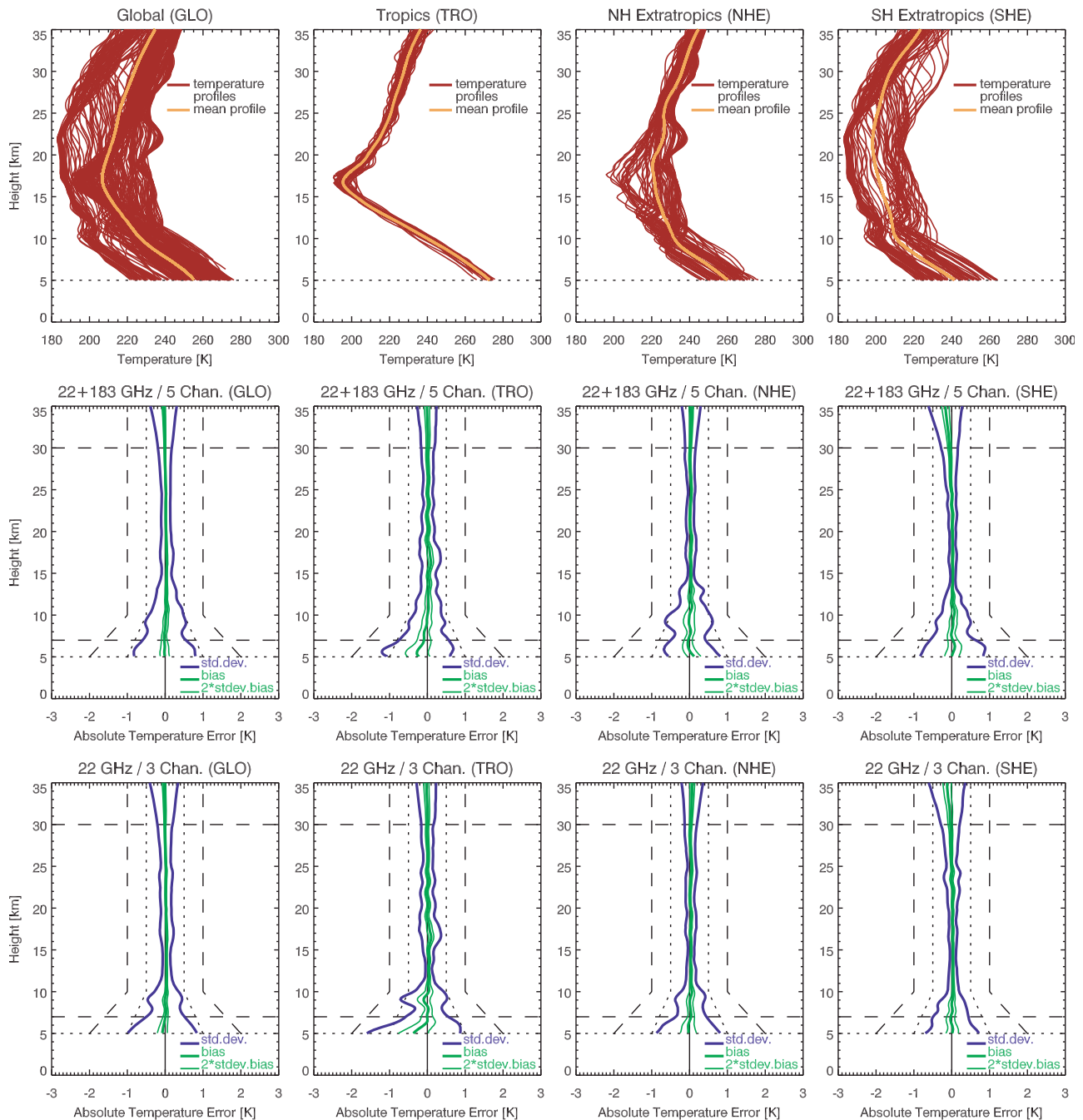


Figure 8. Temperature retrieval performance results in the four regions considered. The layout is the same as in Figure 7 (see Figure 7 caption for explanation).

standard error, and at the same time their RMS error, is found well within the target requirement of 0.5 K at all heights above 10 km and in all four regions. Below 10 km the target requirements are met as well, whereby in the tropics below about 7 km a bias tendency is visible toward 5 km (about 0.3 K near 5 km). The latter is induced by the fact that all measurement channels, including the lowest frequencies at 17.25 GHz and 20.2 GHz, show significant absorption in this humid region near the UTLS bottom and weighting of absorptions and refractivity is not yet optimal there. This is consistent with earlier studies of Schweitzer [2004], which also showed with respect to a possible additional influence

of cloudiness that the overall temperature and humidity retrieval performance above about 5 km is rather insensitive to the presence of clouds. Similarly, while scintillations somewhat increase statistical errors they do not leave biases.

[55] As for pressure, and for the same reasons as explained there, the temperature retrieval performance is essentially independent of the number of channels used, except to some degree below about 15 km, where the different absorption channel weightings play an appreciable role in addition to the refraction information. For example, the “bump” at about 10 km, which is most pronounced in

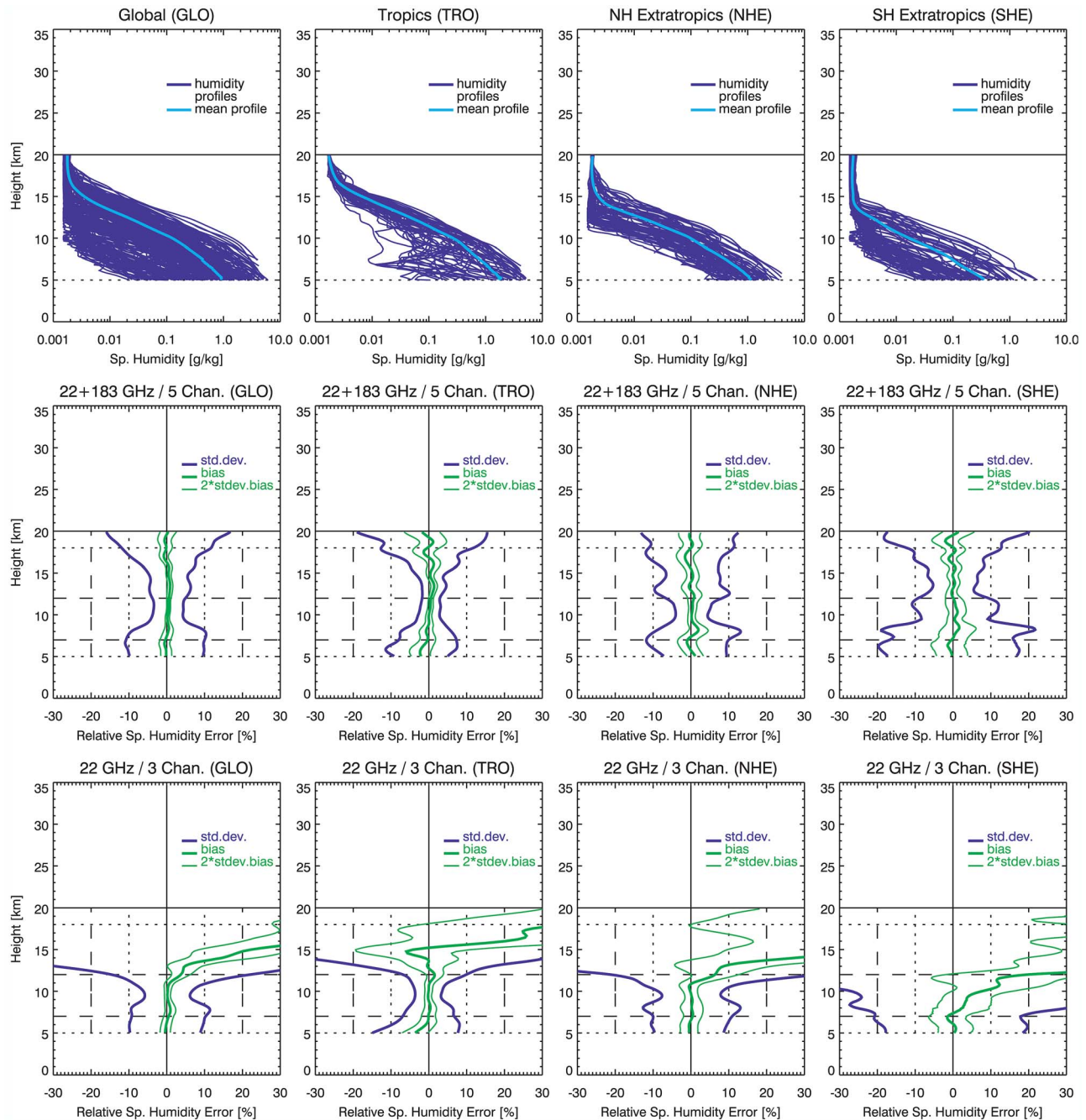


Figure 9. Specific humidity retrieval performance results in the four regions considered. The layout is the same as in Figure 7 (see Figure 7 caption for explanation).

the 22 GHz Case, is due to the inverse-variance weighting of the different channels being not yet optimal around this height. In particular, the feature is caused by the steep downward increase of humidity below the tropopause, entailing via the transmission-based weighting (see section 2.4) a sudden increase of the weight of the information in the differential absorption coefficients from the three frequencies relative to refractivity. The “bump” is therefore least apparent in the SHE region, since the moisture content is lowest there (see Figure 9, top) so that the transition to weighting in of the absorption coefficients is less steep. Since the additional 183 GHz frequencies have sufficient sensitivity

up to about 18 km, the weight is distributed more evenly in the 22 + 183 GHz Case, which is why there appears not such a “bump”-like feature in this case but rather the standard error increases more gradually already from near 15 km downward. Further optimized weighting in future can enhance the retrievals to a further smoothed and improved error profile behavior below about 15 km but given the favorable performance within target requirements already now this is not considered urgent.

[56] Compared to GRO retrieval performance as studied by *Steiner and Kirchengast [2005]* by similar end-to-end simulations, but also the performance from real GRO data is

well understood meanwhile and consistent with those results [e.g., *Steiner et al.*, 2009; *Ho et al.*, 2009], the LMO performance for UTLS temperature and pressure retrieval is similar to GRO, whereby LMO will likely improve on GRO by up to about a factor of 2 plus resolving the temperature-humidity ambiguity. Above 20 km the improvement is expected due to the LMO insensitivity to ionospheric errors, which will in addition extend accurate retrievals to also cover the upper stratosphere superior to GRO. Below about 12 km it is expected due to the LMO capacity to retrieve temperature and pressure without the background information needed by GRO to derive temperature/pressure and humidity from refractivity (also into the lower troposphere if including channels at frequencies <15 GHz and wave optics retrieval).

[57] Figure 9 shows the results for specific humidity, where the UTLS atmospheric variability reasonably embodied by the ensemble of profiles (Figure 9, top) is as expected very strong both as a function of height (about 3 orders of magnitude) and as a function of latitude, season, and local weather conditions (about 1 to 2 orders of magnitude). In numbers, the specific humidity in the global profile ensemble (Figure 9, top left) ranges from about 0.02 g kg^{-1} to 6 g kg^{-1} at a height of 5 km to 0.0015 g kg^{-1} to 0.002 g kg^{-1} at 20 km. Therefore, in contrast to the pressure and temperature retrieval, the performance of humidity retrieval assessed in terms of relative errors significantly depends on the region under consideration, since physically the technique is sensitive to absolute humidity values as visible also from the retrieval algorithm (section 2.4). Hence the moist tropics enable most favorable performance (Figure 9, TRO column), dry extratropical winter conditions least favorable (Figure 9, SHE column). Favorably, also the humidity retrievals appear unbiased in all conditions, whereby in the tropics below 7 km a small bias tendency is visible from the current scheme as for temperature above, for the same reasons as discussed there.

[58] Other than pressure and temperature retrieval the humidity retrieval also strongly depends on whether the 22 GHz Case or the 22 + 183 GHz Case is implemented in an LMO mission design: the two additional channels at the 183 GHz water vapor line with best sensitivity above 10 km (see Figure 6) extend accurate retrievals beyond about 10 to 12 km, where the 22 GHz Case finds its limits, up to near 20 km. The 22 + 183 GHz Case thus is able to meet the target accuracy requirements globally up to 18 km, while the 22 GHz Case achieves this up to 11 km for the target and up to 12 km for the threshold requirements (GLO column). The performance especially in the relatively dry SHE region does not fully stay within the requirements, drawn for visual orientation in all error profile panels, but this is in fact not expected there. The accuracy requirements by *Larsen et al.* [2009] specify to meet the humidity requirements globally; in subglobal regions, especially dry ones where such a specification would not be sensible, they are not required to be met. Evidently, in line with *Kursinski et al.* [2002, 2004, 2009] and *Herman et al.* [2004], a 22 + 183 GHz design is clearly preferable. However, also the (least cost) 22 GHz design following the *ESA* [2004a, 2004b] and the recent ACCURATE concept (in least cost demonstration version) [*Kirchengast et al.*, 2010] reaches sufficiently up in absorption sensitivity, to 10 to 12 km, in order to ensure full sensitivity coverage of

the heights with temperature-humidity ambiguity in GRO refractivity so that the LMO data enable separate retrieval of temperature and humidity beyond the GRO capacity.

[59] We note finally that the humidity retrieval performance found here is worse than the one assessed for the ATOMMS concept [*Kursinski et al.*, 2002, 2004, 2009], which estimates achieving errors lower than 3% in the UTLS and sensitivity well beyond 20 km. The reason is that the ATOMMS concept baselines significantly larger signal-to-noise ratio than assumed here (and thus lower thermal noise) as well as more channels, including near the 183.31 GHz line center in the 182 to 185 GHz band currently reserved by international frequency regulations exclusively for passive sounding. In other words, the LMO three-frequency “minimum” design represented by the 22 GHz Case is for relatively straightforward implementation with available and mature (space) technologies, whereas the ATOMMS concept represents a more ambitious and challenging design for achieving improved performance. We add that, as a difference the other way round, the influence of turbulence on differential transmissions estimated by *Kursinski et al.* [2009] is about twice the influence estimated by *Gorbunov and Kirchengast* [2007]; the parameterization of the scintillation error in this study was based on the latter study. Since the turbulence-induced differential transmission error is very small in both studies (about 1% to 2% near 5 km, decreasing upward), this difference is of minor relevance for the results discussed here. Nevertheless it deserves further understanding and reconciliation for which especially real measurements such as from the upcoming ATOMMS aircraft-to-aircraft occultation demonstration [*Kursinski et al.*, 2009] will be highly useful.

5. Summary and Conclusions

[60] In this study we advanced the understanding and utility of the LEO-LEO microwave occultation (LMO) method, an enhancement of the GPS radio occultation (GRO) technique exploiting in addition to refraction also absorption of microwave signals, in two ways: (1) we introduced a new retrieval algorithm for processing LMO excess phase and amplitude data from multiple frequencies, complementing existing GRO retrieval algorithms anchored on dual-frequency excess phase data; and (2) we employed the algorithm in an ensemble-based end-to-end performance analysis that assessed the accuracy of pressure, temperature, and humidity profiles retrieved from the LMO data. These data were simulated under quasi-realistic conditions (high-resolution ECMWF T511L91 analysis field including 3-D clouds for modeling the atmosphere, high-accuracy 3-D ray tracing, inclusion of errors from turbulence and of reasonable observation system/instrumental errors). The EGOPS5 software [*Kirchengast et al.*, 2007; *Fritzer et al.*, 2010] was used for the purpose and the LMO retrieval algorithm was implemented as part of its occultation processing system (OPS), where (gray literature) reports by *Kirchengast et al.* [2006] and *Gorbunov et al.* [2007] provided first detailed algorithm descriptions.

[61] The study complemented work of *Gorbunov and Kirchengast* [2005, 2007] who investigated effects of turbulence and the wave optics processing performance for bending angle and (differential) transmission retrieval,

whereas here we treated the complete retrieval down to the atmospheric profiles, using a geometric optics approach. The LMO retrieval algorithm includes the well known GRO retrieval chain, which is based on excess phase profiles for at least two frequencies from which the refractivity profile is derived via the intermediate step of bending angle retrieval [e.g., *Kursinski et al.*, 1997]. The amplitude profile measurements, available at each absorption-sensitive microwave frequency chosen, are the key added ingredient of LMO. From these, (differential) transmission profiles are retrieved on top of bending angle and, subsequently, (differential) absorption coefficient profiles on top of refractivity. The joint availability of both refractivity and (differential) absorption coefficient profiles is then used to unambiguously derive the thermodynamic state profiles of pressure, temperature, and humidity by an effective top downward stepping optimal estimation algorithm.

[62] In assessing the retrieval performance based on the end-to-end simulations we compared a “minimum” LMO system design with three frequencies near the 22 GHz water vapor line (17.25 GHz, 20.2 GHz, 22.6 GHz) with an extended one with five frequencies, having two channels near 183 GHz added (179 GHz, 182 GHz). The former is of relevance to (least cost) LMO designs like in the recent ACCURATE concept (in least cost demonstration version) [*Kirchengast et al.*, 2010; G. Kirchengast and S. Schweitzer, submitted manuscript, 2011], the latter to more elaborated designs such as the ATOMMS concept [*Kursinski et al.*, 2009]. The performance results were put into context with observational requirements for temperature and humidity formulated for LMO in a way so that the scientific objectives of contributing to atmosphere and climate research can be met [*Larsen et al.*, 2009; *Kursinski et al.*, 2009]. The focus height domain of both the 22 GHz design and the 22 + 183 GHz design is the upper troposphere/lower stratosphere (UTLS) from 5 to 35 km; thus the performance was assessed in this range. Global performance results were complemented by specific results for tropical and Northern/Southern Hemisphere extratropical regions.

[63] Based on the ensemble of simulated LMO data (and further extensive tests as well as applications elsewhere), the retrieval algorithm introduced was found robust, computationally fast (order 1 min per retrieval on a standard computer of the 2 GHz CPU/2 GB RAM scale), and versatile to adequately process LMO data under all different atmospheric conditions from dry and clear to moist and cloudy air such as contained in the adopted ECMWF T511L91 analysis field. The relatively simple but sensible inverse-variance weighting scheme in the atmospheric profiles retrieval, which governs how the information in refractivity and differential absorption coefficient profiles is distributed to pressure, temperature, and humidity profiles, leads to accurate and essentially unbiased results. Merely in the tropics below 7 km near the UTLS bottom a small bias tendency occurs in temperature (about 0.3 K near 5 km) and humidity (about 3% near 5 km), pointing to further improvement potential of the weighting under these most humid conditions where absorption is strongest. Also some characteristic height variations in the error profiles, such as some small “bumps” in the standard deviation profiles of temperature below about 15 km, can be improved in future by more elaborate weighting. Part of this improvement

could be achieved for example by improved tuning of the current weighting, another part by including error correlations between the (differential) transmissions of neighbor frequencies into the BLUE algorithm. Also a two-step retrieval process could be useful, to estimate the general atmospheric state of an occultation event (moisture, clouds) in a first retrieval step and to use this knowledge in a second step to optimize the weighting and other details of the retrieval procedure. However, since these are incremental improvements on an already very effective algorithm, this is not considered urgent.

[64] The thermodynamic state retrieval performance is found very good, superior to GRO, for all three variables, pressure, temperature, and humidity. The general unbiasedness found for the retrievals (which can be further improved by optimized weighting especially near 5 km in humid regions as well as extended by further channels <15 GHz into the lower troposphere) is key for the climate utility of the data (no time-varying biases; the essentially constant uncertainty from spectroscopic parameters [e.g., *Nielsen et al.*, 2005] was not explicitly treated here). As expected, the strongest advance of LMO over GRO is achieved for humidity, in line with previous results not based on end-to-end simulations by *Kursinski et al.* [2002, 2004, 2009] and *Kirchengast and Hoeg* [2004]. The RMS accuracy of the retrieved profiles is found within observational requirements [*Larsen et al.*, 2009] for all three variables, in general well within the target requirements of <0.2% (pressure), <0.5 K (temperature), and <10% (humidity). Pressure and temperature are expected superior to GRO especially above 20 to 30 km, since ionospheric errors are negligible at the LMO frequencies more than an order of magnitude higher than the GRO ones, and below 10 to 12 km (likely down to the boundary layer if adding frequencies <15 GHz and wave optics retrieval) due to the LMO capacity to retrieve temperature and pressure without the mandatory background information needed by GRO to resolve the temperature-humidity ambiguity. LMO humidity is superior to GRO humidity also due to the latter reason, enabled by the several LMO water vapor absorption channels.

[65] Comparing the 22 GHz three-frequency design with the 22 + 183 GHz five-frequency design, the retrieval performance is not significantly different for pressure and temperature, since for these variables the refractive information plays a dominant role and the absorption information is only relevant up to about 10 to 12 km (up to where the “wet term” in refractivity may have some appreciable contribution [e.g., *Foelsche et al.*, 2008]), which is well covered by the 22 GHz frequencies. Regarding humidity, the two additional channels near the 183 GHz water vapor line with best sensitivity above 10 km substantially extend accurate retrievals beyond 10 to 12 km, where the 22 GHz channels find their limit, up to near 20 km. In line with *Kursinski et al.* [2002, 2004, 2009] and *Herman et al.* [2004] a 22 + 183 GHz design is thus clearly preferable. However, also the (least cost) 22 GHz design reaches sufficiently up in absorption sensitivity in order to ensure full sensitivity coverage of the heights with temperature-humidity ambiguity in GRO, where the LMO data therefore enable separate retrieval of the three thermodynamic variables.

[66] Comparison of the errors estimated in this study with previous ones estimated for the ATOMMS concept [*Kursinski*

et al., 2004, 2009] showed that the pressure and temperature errors, governed by refraction information, are generally consistent but the humidity errors here are significantly higher than estimated for ATOMMS. The reason is that ATOMMS baselines significantly larger signal-to-noise ratios as well as more channels. In this sense the least cost 22 GHz design in this study stands for relatively straightforward implementation with existing mature technologies, whereas the ATOMMS concept represents a more ambitious and challenging design for achieving improved performance.

[67] Looking toward next steps, given the high performance found here for LMO by end-to-end simulations under quasi-realistic conditions, consistent with results of previous studies not based on end-to-end simulations, we are encouraged to further pursue the ACCURATE mission concept combining LMO with the novel LEO-LEO infrared laser occultation. The latter enables complementary profiling of greenhouse gases (water vapor, carbon dioxide, methane, nitrous oxide, etc.) and line-of-sight wind over the UTLS and can for the information it needs on the thermodynamic state ideally draw from simultaneous pressure, temperature, and humidity profiling by LMO (G. Kirchengast and S. Schweitzer, submitted manuscript, 2011). There is thus reasonable hope that a next generation of occultation observing systems may join the successful GPS radio occultation in future, extending its unique refractivity profiling capacity to a much more complete profiling of the atmospheric state, at similar or superior quality, for all thermodynamic, wind, and composition variables included.

[68] **Acknowledgments.** The authors thank U. Foelsche, A. Gobiet, B. Scherllin-Pirscher, A. K. Steiner (all WEGC/UniGraz), J. Ramsauer (TU Graz), and M. Borsche (MPI-M Hamburg) for their valuable contributions to the EGOPSS software, the core tool used for the simulations of this study. Three anonymous reviewers are gratefully acknowledged for their constructive comments that helped to further improve the paper. ECMWF Reading (United Kingdom) kindly provided access to its atmospheric analysis and forecast data. EGOPS was developed by an international consortium led by UniGraz and involving partners at Danish Meteorological Institute (Denmark), Obukhov Institute of Atmospheric Physics (Russia), Chalmers University of Technology (Sweden), University of Bremen (Germany), Meteorological Office (United Kingdom), Terma Elektronik A/S (Denmark), and RUAG Space GmbH (Austria). The major funding for EGOPS work was provided by ESA. Further funding of this work was provided by the Austrian Science Fund (FWF) and the Austrian Aeronautics and Space Agency (FFG-ALR).

References

- Anthes, R. A., et al. (2008), The COSMIC/FORMOSAT-3 mission: Early results, *Bull. Am. Meteorol. Soc.*, *89*, 313–333, doi:10.1175/BAMS-89-3-313.
- Beyerle, G., T. Schmidt, G. Michalak, S. Heise, J. Wickert, and C. Reigber (2005), GPS radio occultation with GRACE: Atmospheric profiling utilizing the zero difference technique, *Geophys. Res. Lett.*, *32*, L13806, doi:10.1029/2005GL023109.
- European Space Agency (ESA) (2004a), *ACE+: Atmosphere and Climate Explorer, 4th Report of Reports for Mission Selection—The Six Candidate Earth Explorer Missions*, ESA SP-1279(4), 60 pp., ESA Publ. Div., Noordwijk, Netherlands.
- European Space Agency (ESA) (2004b), *ACE+: Atmosphere and Climate Explorer Technical and Programmatic Annex, 4th Report of Reports for Mission Selection—The Six Candidate Earth Explorer Missions*, ESA Spec. Publ. Annex to ESA SP-1279(4), 39 pp., ESA Publ. Div., Noordwijk, Netherlands.
- Fjeldbo, G., A. J. Kliore, and V. R. Eshleman (1971), The neutral atmosphere of Venus as studied with the Mariner V radio occultation experiments, *Astron. J.*, *76*, 123–140, doi:10.1086/111096.
- Foelsche, U., and G. Kirchengast (2004), Sensitivity of GNSS radio occultation data to horizontal variability in the troposphere, *Phys. Chem. Earth*, *29*, 225–240, doi:10.1016/j.pce.2004.01.007.
- Foelsche, U., M. Borsche, A. K. Steiner, A. Gobiet, B. Pirscher, G. Kirchengast, J. Wickert, and T. Schmidt (2008), Observing upper troposphere-lower stratosphere climate with radio occultation data from the CHAMP satellite, *Clim. Dyn.*, *31*, 49–65, doi:10.1007/s00382-007-0337-7.
- Fritzer, J., G. Kirchengast, M. Pock, and V. Proschek (2010), End-to-End Generic Occultation Performance Simulation and Processing System version 5.5 (EGOPS 5.5) Software User Manual, *Tech. Rep. ESA/ESTEC 1/2010*, 490 pp., Wegener Cent. and IGAM/Inst. of Phys., Univ. of Graz, Graz, Austria.
- Gershenfeld, N. (1999), *The Nature of Mathematical Modeling*, Cambridge Univ. Press, Cambridge, U. K.
- Giering, R., and T. Kaminski (1998), Recipes for adjoint code construction, *Trans. Math. Software*, *24*, 437–474, doi:10.1145/293686.293695.
- Gobiet, A., and G. Kirchengast (2004), Advancements of Global Navigation Satellite System radio occultation retrieval in the upper stratosphere for optimal climate monitoring utility, *J. Geophys. Res.*, *109*, D24110, doi:10.1029/2004JD005117.
- Gobiet, A., G. Kirchengast, G. L. Manney, M. Borsche, C. Retscher, and G. Stiller (2007), Retrieval of temperature profiles from CHAMP for climate monitoring: Intercomparison with Envisat MIPAS and GOMOS and different atmospheric analyses, *Atmos. Chem. Phys.*, *7*, 3519–3536, doi:10.5194/acp-7-3519-2007.
- Gorbunov, M. E. (2002), Canonical transform method for processing radio occultation data in the lower troposphere, *Radio Sci.*, *37*(5), 1076, doi:10.1029/2000RS002592.
- Gorbunov, M. E., and G. Kirchengast (2005), Processing X/K band radio occultation data in the presence of turbulence, *Radio Sci.*, *40*, RS6001, doi:10.1029/2005RS003263.
- Gorbunov, M. E., and G. Kirchengast (2007), Fluctuations of radio occultation signals in X/K band in the presence of anisotropic turbulence and differential transmission retrieval performance, *Radio Sci.*, *42*, RS4025, doi:10.1029/2006RS003544.
- Gorbunov, M. E., and K. B. Lauritsen (2004), Analysis of wave fields by Fourier integral operators and their application for radio occultations, *Radio Sci.*, *39*, RS4010, doi:10.1029/2003RS002971.
- Gorbunov, M. E., S. S. Leroy, and G. Kirchengast (2007), Retrieval of complex refractivity, temperature, and humidity from radio occultation data in X/K band, *Tech. Rep. ESA/ESTEC 5/2007*, Wegener Cent., Univ. of Graz, Graz, Austria.
- Haji, G. A., C. O. Ao, P. A. Iijima, D. Kuang, E. R. Kursinski, A. J. Mannucci, T. K. Meehan, L. J. Romans, M. de la Torre Juarez, and T. P. Yunck (2004), CHAMP and SAC-C atmospheric occultation results and intercomparisons, *J. Geophys. Res.*, *109*, D06109, doi:10.1029/2003JD003909.
- Healy, S. B., and J.-N. Thépaut (2006), Assimilation experiments with CHAMP GPS radio occultation measurements, *Q. J. R. Meteorol. Soc.*, *132*, 605–623, doi:10.1256/qj.04.182.
- Herman, B. M., E. R. Kursinski, D. Feng, D. Ward, S. Syndergaard, and E. Lane (2003), Active Tropospheric Ozone and Moisture Sounder (ATOMS), *Sci. Rep. NASA Contract NAS1-99055*, Inst. of Atmos. Phys., Univ. of Ariz., Tucson.
- Herman, B. M., D. Feng, D. Flittner, E. R. Kursinski, S. Syndergaard, and D. Ward (2004), An overview of the Univ. of Arizona ATOMS project, in *Occultations for Probing Atmosphere and Climate*, edited by G. Kirchengast et al., pp. 189–200, Springer, Berlin.
- Ho, S.-P., et al. (2009), Estimating the uncertainty of using GPS radio occultation data for climate monitoring: Inter-comparison of CHAMP refractivity climate records 2002–2006 from different data centers, *J. Geophys. Res.*, *114*, D23107, doi:10.1029/2009JD011969.
- Jensen, A. S., M. S. Lohmann, H.-H. Benzon, and A. S. Nielsen (2003), Full spectrum inversion of radio occultation signals, *Radio Sci.*, *38*(3), 1040, doi:10.1029/2002RS002763.
- Jensen, A. S., M. S. Lohmann, A. S. Nielsen, and H.-H. Benzon (2004), Geometrical optics phase matching of radio occultation signals, *Radio Sci.*, *39*, RS3009, doi:10.1029/2003RS002899.
- Kirchengast, G. (2004), Occultations for probing atmosphere and climate: Setting the scene, in *Occultations for Probing Atmosphere and Climate*, edited by G. Kirchengast et al., pp. 1–8, Springer, Berlin.
- Kirchengast, G., and P. Hoeg (2004), The ACE+ mission: An Atmosphere and Climate Explorer based on GPS, Galileo, and LEO-LEO radio occultation, in *Occultations for Probing Atmosphere and Climate*, edited by G. Kirchengast et al., pp. 201–220, Springer, Berlin.
- Kirchengast, G., J. Fritzer, M. Schwaerz, S. Schweitzer, and L. Kornbluh (2004), The Atmosphere and Climate Explorer mission ACE+: Scientific

- algorithms and performance overview, *Tech. Rep. ESA/ESTEC 2/2004*, Inst. for Geophys. Astrophys. and Meteorol., Univ. of Graz, Graz, Austria.
- Kirchengast, G., S. Schweitzer, M. Schwaerz, J. Fritzer, and M. Gorbunov (2006), Advanced retrieval processing chain for derivation of atmospheric profiles from LEO-LEO radio occultation data, *Tech. Rep. ESA/ESTEC 2/2006*, Wegener Cent., Univ. of Graz, Graz, Austria.
- Kirchengast, G., S. Schweitzer, J. Ramsauer, and J. Fritzer (2007), End-to-End Generic Occultation Performance Simulator version 5.2 (EGOPsv5.2) Software User Manual (Overview, Reference, and File Format Manual), *Tech. Rep. ESA/ESTEC 4/2007*, Wegener Cent. and IGAM/Inst. of Phys., Univ. of Graz, Graz, Austria.
- Kirchengast, G., et al. (2010), ACCURATE—climate benchmark profiling of greenhouse gases and thermodynamic variables and wind from space (ESA Earth Explorer Opportunity Mission EE-8 Proposal), *Sci. Rep. 36-2010*, Wegener Cent., Graz, Austria.
- Kursinski, E. R., G. A. Hajj, J. T. Schofield, R. P. Linfield, and K. R. Hardy (1997), Observing Earth's atmosphere with radio occultation measurements using the Global Positioning System, *J. Geophys. Res.*, *102*, 23,429–23,465, doi:10.1029/97JD01569.
- Kursinski, E. R., G. A. Hajj, S. S. Leroy, and B. Herman (2000), The GPS radio occultation technique, *Terr. Atmos. Ocean Sci.*, *11*, 53–114.
- Kursinski, E. R., S. Syndergaard, D. Flittner, D. Feng, G. Hajj, B. Herman, D. Ward, and T. Yunck (2002), A microwave occultation observing system optimized to characterize atmospheric water, temperature, and geopotential via absorption, *J. Atmos. Oceanic Technol.*, *19*, 1897–1914, doi:10.1175/1520-0426(2002)019<1897:AMOO>2.0.CO;2.
- Kursinski, E. R., D. Feng, D. Flittner, G. Hajj, B. Herman, F. Romberg, S. Syndergaard, D. Ward, and T. Yunck (2004), An active microwave limb sounder for profiling water vapor, ozone, temperature, geopotential, clouds, isotopes and stratospheric winds, in *Occultations for Probing Atmosphere and Climate*, edited by G. Kirchengast et al., pp. 173–187, Springer, Berlin.
- Kursinski, E. R., D. Ward, A. Otarola, K. Frehlich, C. Groppi, S. Albanna, M. Shein, W. Bertiger, H. Pickett, and M. Ross (2009), The Active Temperature, Ozone and Moisture Microwave Spectrometer (ATOMMS), in *New Horizons in Occultation Research*, edited by A. K. Steiner et al., pp. 295–313, Springer, Berlin, doi:10.1007/978-3-642-00321-9_24.
- Larsen, G. B., G. Kirchengast, and P. Bernath (2009), Science objectives and observational requirements of the ACCURATE mission concept, *Tech. Rep. DMI/ESA-IRDAS/ObsReq/Oct2009*, Danish Meteorol. Inst., Copenhagen.
- Leroy, S. S. (1997), The measurement of geopotential heights by GPS radio occultation, *J. Geophys. Res.*, *102*, 6971–6986, doi:10.1029/96JD03083.
- Lesne, O., J. Haase, G. Kirchengast, J. Ramsauer, and W. Poetzi (2002), Sensitivity analysis for airborne sounding of the troposphere by GNSS radio occultation, *Phys. Chem. Earth*, *27*, 291–299.
- Liebe, H. J. (1989), MPM—An atmospheric millimeter-wave propagation model, *Int. J. Infrared Millimeter Waves*, *10*, 631–650, doi:10.1007/BF01009565.
- Liebe, H. J., G. A. Hufford, and M. G. Cotton (1993), Propagation modeling of moist air and suspended water/ice particles at frequencies below 1000 GHz, in *AGARD Proceedings: Atmospheric Propagation Effects through Natural and Man-Made Obscurants for Visible to MM-Wave Radiation*, edited by A. Delfour et al., pp. 3–1–3–10, NTIA, Boulder, Colo.
- Luntama, J.-P., G. Kirchengast, M. Borsche, U. Foelsche, A. K. Steiner, S. Healy, A. von Engeln, E. O'Clérigh, and C. Marquardt (2008), Prospects of the EPS GRAS mission for operational atmospheric applications, *Bull. Am. Meteorol. Soc.*, *89*, 1863–1875, doi:10.1175/2008BAMS2399.1.
- Lusignan, B., G. Modrell, A. Morrison, J. Pomalaza, and S. G. Ungar (1969), Sensing the Earth's atmosphere with occultation satellites, *Proc. IEEE*, *57*, 458–467, doi:10.1109/PROC.1969.7000.
- Nielsen, A. S., et al. (2005), Characterization of ACE+ LEO-LEO radio occultation measurements, *DMI-IEP-CUT Tech. Rep. ESA/ESTEC Contract 16743/02/NL/FF*, Danish Meteorol. Inst., Copenhagen.
- Olsen, R. L., D. V. Rogers, and D. B. Hodge (1978), The aR^b relation in the calculation of rain attenuation, *IEEE Trans. Antennas Propag.*, *26*, 318–329, doi:10.1109/TAP.1978.1141845.
- Rieder, M. J., and G. Kirchengast (2001), Error analysis and characterization of atmospheric profiles retrieved from GNSS occultation data, *J. Geophys. Res.*, *106*, 31,755–31,770, doi:10.1029/2000JD000052.
- Rocken, C., et al. (1997), Analysis and validation of GPS/MET data in the neutral atmosphere, *J. Geophys. Res.*, *102*, 29,849–29,866, doi:10.1029/97JD02400.
- Rodgers, C. D. (2000), *Inverse Methods for Atmospheric Sounding: Theory and Practice*, World Sci., Singapore.
- Salby, M. L. (1996), *Fundamentals of Atmospheric Physics*, Academic, San Diego, Calif.
- Schwaerz, M., J. Ramsauer, and G. Kirchengast (2006), End-to-end scientific performance analysis for retrieval of atmospheric data from Galileo K-band radio links, *Tech. Rep. EU/GJU 1/2006*, Wegener Center, Univ. of Graz, Graz, Austria.
- Schweitzer, S. (2004), Atmosphere and Climate Explorer mission ACE+: Humidity and temperature retrieval performance analysis (M.S. thesis), *IGAM Wiss. Ber. 20*, Inst. for Geophys. Astrophys. and Meteorol., Univ. of Graz, Graz, Austria.
- Schweitzer, S. (2010), The ACCURATE concept and the infrared laser occultation technique: Mission design and assessment of retrieval performance (Ph.D. thesis), *Sci. Rep. 34-2010*, Wegener Cent., Graz, Austria.
- Smith, E. K., and S. Weintraub (1953), The constants in the equation for atmospheric refractive index at radio frequencies, *Proc. IRE*, *41*, 1035–1037.
- Sofieva, V. F., and E. Kyrölä (2004), Abel integral inversion in occultation measurements, in *Occultations for Probing Atmosphere and Climate*, edited by G. Kirchengast et al., pp. 77–85, Springer, Berlin.
- Sokolovskiy, S. V. (2000), Inversions of radio occultation amplitude data, *Radio Sci.*, *35*, 97–105, doi:10.1029/1999RS002203.
- Steiner, A. K., and G. Kirchengast (2004), Ensemble-based analysis of errors in atmospheric profiles retrieval from GNSS occultation data, in *Occultations for Probing Atmosphere and Climate*, edited by G. Kirchengast et al., pp. 149–160, Springer, Berlin.
- Steiner, A. K., and G. Kirchengast (2005), Error analysis for GNSS radio occultation data based on ensembles of profiles from end-to-end simulations, *J. Geophys. Res.*, *110*, D15307, doi:10.1029/2004JD005251.
- Steiner, A. K., G. Kirchengast, and H. P. Ladreiter (1999), Inversion, error analysis, and validation of GPS/MET occultation data, *Ann. Geophys.*, *17*, 122–138.
- Steiner, A. K., A. Loescher, and G. Kirchengast (2006), Error characteristics of refractivity profiles retrieved from CHAMP radio occultation data, in *Atmosphere and Climate: Studies by Occultation Methods*, edited by U. Foelsche et al., pp. 27–36, Springer, Berlin.
- Steiner, A. K., G. Kirchengast, B. C. Lackner, B. Pirscher, M. Borsche, and U. Foelsche (2009), Atmospheric temperature change detection with GPS radio occultation 1995 to 2008, *Geophys. Res. Lett.*, *36*, L18702, doi:10.1029/2009GL039777.
- Syndergaard, S., D. E. Flittner, E. R. Kursinski, D. D. Feng, B. M. Herman, and D. M. Ward (2004), Simulating the influence of horizontal gradients on retrieved profiles from ATOMS occultation measurements—a promising approach for data assimilation, in *Occultations for Probing Atmosphere and Climate*, edited by G. Kirchengast et al., pp. 221–232, Springer, Berlin.
- Ware, R., et al. (1996), GPS Sounding of the atmosphere from low Earth orbit: Preliminary results, *Bull. Am. Meteorol. Soc.*, *77*, 19–40, doi:10.1175/1520-0477(1996)077<0019:GSOTAF>2.0.CO;2.
- Wickert, J., T. Schmidt, G. Beyerle, R. König, C. Reigber, and N. Jakowski (2004), The radio occultation experiment aboard CHAMP: Operational data analysis and validation of vertical atmospheric profiles, *J. Meteorol. Soc. Jpn.*, *82*, 381–395, doi:10.2151/jmsj.2004.381.
- Yunck, T. P., G. A. Hajj, E. R. Kursinski, J. A. LaBrecque, S. T. Lowe, M. M. Watkins, and C. McCormick (2000), AMORE: An autonomous constellation concept for atmospheric and ocean observation, *Acta Astronaut.*, *46*, 355–364, doi:10.1016/S0094-5765(99)00231-3.

J. Fritzer, M. E. Gorbunov, G. Kirchengast, M. Schwaerz, and S. Schweitzer, Wegener Center for Climate and Global Change, University of Graz, Leechgasse 25, 8010 Graz, Austria.